

AD-A268 072 INFORMATION PAGE

Form Approved
OMB No. 0704-0186



Allow an average of 1 hour per response, including the time for reviewing instructions, searching existing data sources, gathering the collection of information, sending comments regarding this burden estimate or any other aspect of this burden to Washington Headquarters Services, Directorate for Information Operations and Reports, 1215 Jefferson Office of Management and Budget, Paperwork Reduction Project (0704-0186), Washington, DC 20503.

1. REPORT DATE August 1993		3. REPORT TYPE AND DATES COVERED THESIS/DISSERTATION	
4. TITLE AND SUBTITLE AN EMPIRICAL STUDY OF TROPICAL CLOUD CLUSTERS USING SPECIAL SENSOR MICROWAVE IMAGER DATA		5. FUNDING NUMBERS	
6. AUTHOR(S) Maj Mark P. Weadon		8. PERFORMING ORGANIZATION REPORT NUMBER AFIT/CI/CIA- 93-120	
7. PERFORMING ORGANIZATION NAME(S) AND ADDRESS(ES) AFIT Student Attending: Pennsylvania State University		10. SPONSORING / MONITORING AGENCY REPORT NUMBER	
9. SPONSORING / MONITORING AGENCY NAME(S) AND ADDRESS(ES) DEPARTMENT OF THE AIR FORCE AFIT/CI 2950 P STREET WRIGHT-PATTERSON AFB OH 45433-7765		11. SUPPLEMENTARY NOTES	
12a. DISTRIBUTION / AVAILABILITY STATEMENT Approved for Public Release IAW 190-1 Distribution Unlimited MICHAEL M. BRICKER, SMSgt, USAF Chief Administration		12b. DISTRIBUTION CODE	
13. ABSTRACT (Maximum 200 words)			
<p>DTIC ELECTE AUG 17 1993</p> <p>S A D</p> <p>93-19044</p>			
14. SUBJECT TERMS		15. NUMBER OF PAGES 92	
		16. PRICE CODE	
17. SECURITY CLASSIFICATION OF REPORT	18. SECURITY CLASSIFICATION OF THIS PAGE	19. SECURITY CLASSIFICATION OF ABSTRACT	20. LIMITATION OF ABSTRACT

The Pennsylvania State University

The Graduate School

15-1-93

**AN EMPIRICAL STUDY OF TROPICAL CLOUD CLUSTERS
USING SPECIAL SENSOR MICROWAVE IMAGER DATA**

A Thesis in

Meteorology

by

Mark P. Weadon

Accession For	
NTIS CRA&I	<input checked="" type="checkbox"/>
DTIC TAB	<input type="checkbox"/>
Unannounced	<input type="checkbox"/>
Justification	
By	
Distribution/	
Availability Codes	
Dist	Avail and/or Special
A-1	

**Submitted in Partial Fulfillment
of the Requirements
for the Degree of**

DTIC QUALITY INSPECTED 3

Master of Science

August 1993

We approve the thesis of Mark P. Weadon.

Date of Signature



Judith A. Curry
Associate Professor of Meteorology
Thesis Advisor

13 May 93



Thomas P. Ackerman
Associate Professor of Meteorology

20 May 1993



Dennis W. Thomson
Professor of Meteorology
Head of the Department of
Meteorology

21 May 93

I grant The Pennsylvania State University the nonexclusive right to use this work for the University's own purposes and to make single copies of the work available to the public on a not-for-profit basis if copies are not otherwise available.



Mark P. Weadon

ABSTRACT

Fifteen cases of Tropical Cloud Clusters (TCCs) in the western Pacific were analyzed using infrared satellite imagery and microwave satellite data from the Special Sensor Microwave Imager (SSM/I). Microwave data yielded atmospheric parameters of integrated water vapor, liquid water path, ice water path, and surface rainrate. Analyzed fields of SSM/I-derived parameters were then compared with each other and with infrared blackbody cloud top temperatures of TCCs in various stages of development.

It was found that TCCs form preferentially in regions of elevated integrated water vapor. It is hypothesized that this extremely humid pre-storm environment signals large scale ascent, contributing to favorable conditions for tropical convection. Areas of surface precipitation retrieved from SSM/I were found, in general, to correlate to infrared cloud top temperatures of $< -65^{\circ}\text{C}$, though the coldest cloud tops did not necessarily coincide with the heaviest rain. It was found that the microwave signature of a TCC changes over the course of its life cycle, from a balance of liquid water emission and ice scattering in the intensifying and mature phases, to a predominance of liquid water emission over ice scattering in the dissipating phase.

TABLE OF CONTENTS

LIST OF FIGURES	vi
LIST OF TABLES	x
ACKNOWLEDGMENTS	xi
Chapter 1. INTRODUCTION	1
Chapter 2. DATA AND METHODOLOGY	6
2.1 Data	6
2.2 Methodology	9
Chapter 3. GEOPHYSICAL PROPERTIES OF MICROWAVE RADIATION	13
3.1 Emission by Atmospheric Gases	13
3.2 Emission by Earth's Surface	15
3.3 Emission and Scattering by Clouds and Hydrometeors	20
3.4 An Example	26
Chapter 4. ALGORITHMS FOR RETRIEVAL OF ATMOSPHERIC PARAMETERS	39
4.1 Column Integrated Water Vapor	39
4.2 Normalized Polarization at 37 GHz	43
4.3 Liquid Water Path	44
4.4 Polarization Corrected Temperature at 85 GHz	47
4.5 Ice Water Path	49
4.6 Rainfall	50
Chapter 5. CASE STUDIES	53
5.1 TCC of 13 November 1987--Formative and Mature Phases	53
5.2 TCC of 16 November 1987--Intensifying Phase	68
5.3 TCC of 21 November 1987--Dissipating Phase	74
Chapter 6. DISCUSSION	81
Chapter 7. CONCLUSION AND RECOMMENDATIONS FOR FURTHER STUDY	86

TABLE OF CONTENTS (CONT'D)

REFERENCES 88

LIST OF FIGURES

1.	Total atmospheric microwave transmission for a zenith angle of 53°. Model atmospheres used are (1) wintertime polar, (2) summertime polar, (3) wintertime midlatitude, (4) summertime midlatitude, and (5) tropical. Source: Petty (1990)	14
2.	Typical SSM/I brightness temperatures plotted as functions of total atmospheric water vapor V . Atmospheric temperature and other parameters are allowed to vary with V . No cloud water is assumed. Source: Petty (1990)	17
3.	Cross section of SSM/I clear-sky radiance values in western Pacific: 13 November 1987 1927 UTC. Along Equator	19
4.	Schematic depiction of how 37 GHz brightness temperatures change with increasing rain rate and/or cloud opacity. Horizontal axis is $\Delta TB \equiv (TBV - TBH)$; vertical axis is $TB_{AV} \equiv (TBV + TBH)/2$. Numbers on curves indicate rainrates in mm/hr. Source: Spencer (1986)	21
5.	GMS unenhanced IR: 14 November 1987 2130 UTC	26
6.	Average brightness temperature and polarization at 37 GHz: 14 November 1987 2056 UTC. From 3°N to 8°N and 155°E to 160°E	27
7.	Average brightness temperature and polarization at 19 GHz: 14 November 1987 2056 UTC. From 3°N to 8°N and 155°E to 160°E	29
8.	Average brightness temperature and polarization at 85 GHz: 14 November 1987 2056 UTC. From 3°N to 8°N and 155°E to 160°E	31
9.	Cross section of radiance values at 19H and 19V: 14 November 1987 2056 UTC. Along 157°E	33
10.	Cross section of radiance values at 37H and 37V: 14 November 1987 2056 UTC. Along 157°E	34

11.	Cross section of radiance values of 85H and 85V: 14 November 1987 2056 UTC. Along 157°E	35
12.	Cross section of radiance values at 85H and 85V (high resolution): 14 November 1987 2056 UTC. Along 157°E.....	37
13.	Comparison of SSM/I-derived with RAOB-derived values of integrated water vapor V	42
14a-d.	GMS IR Temperatures: 13 November 1987. Contours for -65°C, -75°C, and -85°C. (a) 0630 UTC (b) 1230 UTC (c) 1530 UTC (d) 1830 UTC	54
15a-d.	SSM/I-derived parameters: 13 November 1987 0648 UTC. (a) Integrated water vapor. Units in kg/m ² . (b) Rainfall. Contours for 0 and 4 mm/hr. (c) Liquid water path. Contours for 500, 1000, 2000 g/m ² . (d) Ice water path. Contours for 30, 60, 90 g/m ²	57
16.	GMS unenhanced IR: 13 November 1987 0330 UTC	59
17.	Cross section of LWP and IWP: 13 November 0648 UTC. Along 4.56°S	59
18.	Cross section of PCT: 13 November 1987 0648 UTC. Along 4.56°S	60
19.	GMS unenhanced IR: 13 November 2130 UTC	61
20a.	SSM/I-derived parameters: 13 November 1987 1927 UTC. Integrated water vapor. Units in kg/m ²	61
20b-e.	SSM/I-derived parameters: 13 November 1987 1927 UTC (b) Rainfall. Contours for 0, 6, 12 mm/hr. (c) Polarization corrected temperature. Contours for 250°, 230°, 210°K. (d) Liquid water path. Contours for 500, 2000, 4000 g/m ² . (e) Ice water path. Contours for 60, 120 g/m ²	62
21.	Cross section of LWP and IWP: 13 November 1927 UTC. Along 4.5°S	65

22.	Cross section of PCT: 13 November 1987 1927 UTC. Along 4.5°S	65
23.	PCT/19H scatter plot: 13 November 1927 UTC. From 6°S to Equator and 162°E to 168°E. Numbers are rainrates in mm/hr	66
24.	PCT/19H scatter plot: 13 November 0648 UTC. From 7°S to Equator and 165°E to 173°E. Numbers are rainrates in mm/hr	68
25.	GMS unenhanced IR: 16 November 1987 2130 UTC	69
26a-b.	GMS IR temperatures: 16 November 1987. Contours for -65°C, C, -75°C, -85°C. (a) 1830 UTC (b) 2130 UTC	69
27a-d.	SSM/I-derived parameters: 16 November 1987 1850 UTC. (a) Rainfall. Contours for 0, 6, 12 mm/hr. (b) Polarization corrected temperature. Contours for 250°, 230°, 210°K. (c) Liquid water path. Contours for 1000, 2000, 3000, 4000 g/m ² . (d) Ice water path. Contours for 50, 100, 150 g/m ²	71
28.	Cross section of LWP and IWP: 16 November 1987 1850 UTC. Along 167.8°E	73
29.	Cross section of PCT: 16 November 1987 1850 UTC. Along line 167.8°E	73
30.	PCT/19H scatter plot: 16 November 1987 1850 UTC. From 4°N to 8°N and 165°E to 169°E. Numbers are rainrates in mm/hr	74
31.	GMS unenhanced IR: 21 November 1987 2130 UTC	75
32a-b.	GMS IR temperatures: 21 November 1987. Contours for -65°C, -75°C. (a) 1830 UTC (b) 2130 UTC	76
33a-d.	SSM/I-derived parameters: 21 November 1987 1930 UTC. (a) Rainfall. Contours for 0, 4, 8 mm/hr. (b) Polarization corrected temperature. Contour for 250°K. (c) Liquid water path contours for 1000, 2000, 3000, 4000 g/m ² . (d) Ice water path. Contour for 30 g/m ²	77

34. Cross section of LWP and IWP: 21 November 1987 1930 UTC. Along 152.6°E	79
35. Cross section of PCT: 21 November 1930 UTC. Along 152.6°E	79
36. PCT/19H scatter plot: 21 November 1930 UTC. From 1°N to 7°N and 151°E to 154°E. Numbers are rainrates in mm/hr	80
37a-c. Composite PCT/19H scatter plots. Numbers are rainrates in mm/hr. (a) Formative TCCs. (b) Mature TCCs. (c) Dissipating TCCs	82
38a-c. Schematic of a tropical cloud cluster in three successive stages of development. (a) Formative stage consisting of convective cells. (b) Mature stage. Cloud shield covers area A_c , convective cells are located in area A_n , stratiform precipitation falling from mid-level cloud base within area A_s and A_o is covered by upper-level cloud overhang. (c) Dissipating stage in which convective cells have disappeared and weak stratiform precipitation is not reaching ground. Upper panels of (a) - (c) are plan views. Lower panels are vertical cross sections. Source: Houze (1982)	84

LIST OF TABLES

1. Specifications of the F8 SSM/I. Source: Hollinger (1987) 7
2. Size parameter of variable-size drops at a range of microwave frequencies. The table is divided into a Rayleigh regime (upper left) and a Mie regime (lower right, *italic*) using a 0.2 size-parameter threshold. Source: Smith *et al.* (1991) 24

ACKNOWLEDGMENTS

I wish to thank Professor Judy Curry for her encouragement and guidance throughout this research project, even though at long distance. To Professor Mike Fritsch I owe a debt of gratitude for his insights and critical scrutiny along the way. Guosheng Liu and Rong Sheu, who assisted me with programming tasks far beyond my capabilities, were instrumental in the timely completion of the project. Finally, thanks go to my wife Anne, not only for her tangible assistance in preparing this manuscript, but for her love and support in all my academic endeavors.

This research was supported by the National Science Foundation (grant number ATM-9223150).

CHAPTER 1

INTRODUCTION

Tropical Cloud Clusters (TCCs), as is apparent from satellite imagery, are the dominant species of precipitating weather system in the tropics. The undilute "hot towers" postulated by Riehl and Simpson (1958) as necessary to balance the global heat budget rarely appear as discrete cumulonimbus cells, but rather tend to organize themselves into larger scale (100-1000 km) mesoscale ensembles. TCCs occasionally form the core of convection from which tropical cyclones may evolve. These ensembles consist of both convective and stratiform clouds evolving through stages of growth and decay. The defining satellite signature of the TCC is a large cirrus shield, within which is typically found one or more mesoscale rain areas attaining a maximum horizontal dimension 100-500 km (see Houze and Hobbs, 1982).

Because of their importance to the global heat budget, TCCs have received considerable study over the last 20 years. Ruprecht and Gray (1976) first described the mean synoptic conditions favorable to TCC growth in the Pacific by comparing infrared satellite imagery with rawinsonde data. Field experiments such as GATE and MONEX gathered high-density data which allowed researchers to derive vertical profiles of heat, moisture, and momentum within a cluster (Frank, 1978; Leary and Houze, 1979; Gamache and Houze, 1983). Microphysical processes within

clusters were inferred from *in situ* aircraft measurements during field experiments (Houze and Churchill, 1984).

Based on radar data from GATE and MONEX, Houze (1982) identified four stages in the life cycle of the TCC, a classification generally adopted in subsequent research. A *formative stage* is initiated when dynamic forcing, such as low level convergence from a land breeze or outflow boundaries from prior convection, triggers ascent in the conditionally unstable airmass. This is followed by the growth of several adjacent cumulonimbus cells, either randomly (non-squall type), or linearly distributed (squall type). The *intensifying stage* commences when older cumulonimbus cells grow and merge amidst newer convective cells. Gradually a continuous rain area forms, comprised of both convective and stratiform features. Stratiform precipitation falls from a spreading mid- to upper-level cloud shield which covers the entire cluster. During the *mature phase* the cirrus canopy continues to grow in areal extent. Stratiform precipitation is enhanced by the generation of mid-level convergence, driving mesoscale ascent in the cirrus canopy and mesoscale descent below the freezing level. The *dissipating phase* is characterized by continued stratiform precipitation, mesoscale ascent in the upper troposphere, and gradually diminishing convection.

This description of life cycle, it should be noted, is derived from radar data gathered close to large land masses. Verifying its validity in the open

ocean of the west Pacific, one of the most active convective regions in the world, is difficult at best. In the past, infrared and visible satellite imagery has been relied on almost exclusively for the study of oceanic tropical convection. However, the utility of conventional satellite data in analyzing these systems is limited due to the thick cirrus canopy that obscures underlying precipitation features. Satellite techniques to distinguish convective from stratiform regions by analyzing gradients of cloud top temperatures (see Adler and Negri, 1988) are less effective when the cirrus canopy is extremely thick, as in tropical clusters. Because of the generally low updraft speeds in tropical oceanic convection (LeMone and Zipser, 1980), convective tops rarely penetrate the canopy, which most often appears in IR imagery as a smooth, cold surface.

The DOD's Defense Meteorological Satellite Program's (DMSP) Special Sensor Microwave Imager (SSM/I), launched in 1987, has unique advantages over other satellite sensors, particularly in the study of tropical weather systems. Unlike infrared and visible satellite sensors, which only respond to radiation from the top cloud layer, SSM/I detects microphysical processes *within* the cloud, at levels where precipitation is being formed. Delineating precipitation areas and determining rainfall amounts from IR satellite imagery is a highly inferential procedure, based as it is on the questionable assumption that cloud top temperatures correlate to rainfall intensity below. By contrast, data from microwave radiometers bear a much

more direct relationship to precipitation intensity. The capability to detect hydrometeors below an obscuring cirrus layer makes microwave radiometry a promising medium for the study of tropical weather systems. Moreover, the 7 channels of SSM/I each respond differently to the same precipitating regime, allowing discrimination of microphysical processes at various levels within a cloud.

Most of the copious research on microwave radiometry in recent years has been devoted to developing algorithms for the retrieval of atmospheric parameters. Practical applications of validated microwave algorithms have, for the most part, been confined to the retrieval of temporally averaged values for climatological studies (e.g. Grody *et al.*, 1980; Prabhakara *et al.*, 1983; Chang *et al.*, 1984; Tjemkes *et al.*, 1991; Shin *et al.*, 1990). Aside from climatological studies, surprisingly little has been done to apply microwave algorithms to the study of particular weather systems, in a manner analogous to infrared and visible satellite studies. The few published case studies using microwave data have been devoted to mid-latitude continental convection (Spencer *et al.*, 1989), mid-latitude frontal systems (McMurdie and Katsaros, 1985; Katsaros and Lewis, 1986), and tropical cyclones (Liu *et al.*, 1993). Petty and Katsaros (1989) used data from the earlier Scanning Multichannel Microwave Radiometer to analyze precipitation patterns in a TCC near north coast of Australia from Winter MONEX. It would seem from the scarcity of published studies that the full potential of

SSM/I as an analytical tool in understanding particular weather systems has yet to be realized.

In the following study, SSM/I data will be used in attempting to answer these questions:

- **How do the areas of precipitation in a TCC correlate to the IR temperature of the cloud shield?**
- **Is the life cycle postulated by Houze (1982) valid for TCCs of the western Pacific?**
- **What atmospheric parameters characterize the pre- and post-storm environment of TCCs?**
- **How does the microphysical profile of a TCC change in the course of development?**

To provide the empirical base for answering these questions, 15 western Pacific TCCs have been selected for study. First, data and methodology will be explained. This section will be followed by a brief summary of radiative principles essential to all microwave retrieval algorithms. Then, particular algorithms selected for this study will be explained. Four case studies will then be presented, each representing a TCC in a particular stage of development. Finally, results from the individual case studies will be discussed, including an overview of unresolved issues and recommendations for future study.

would seem from the scarcity of published studies that the full potential of SSM/I as an analytical tool in understanding particular weather systems has yet to be realized.

In the following study, SSM/I data will be used in attempting to answer these questions:

- How do the areas of precipitation in a TCC correlate to the IR temperature of the cloud shield?
- Is the life cycle postulated by Houze (1982) valid for TCCs of the western Pacific?
- What atmospheric parameters characterize the pre- and post-storm environment of TCCs?
- How does the microphysical profile of a TCC change in the course of development?

To provide the empirical base for answering these questions, 15 western Pacific TCCs have been selected for study. First, data and methodology will be explained. This section will be followed by a brief summary of radiative principles essential to all microwave retrieval algorithms. Then, particular algorithms selected for this study will be explained. Four case studies will then be presented, each representing a TCC in a particular stage of development. Finally, results from the individual case studies will be discussed, including an overview of unresolved issues and recommendations for future study.

CHAPTER 2

DATA AND METHODOLOGY

2.1 Data

For this empirical study, 15 tropical cloud clusters were selected from the period October through November 1987. Each cluster met certain IR-based thresholds and was substantially covered by an SSM/I data swath during some period in its evolution.

Initial identification of clusters and cloud was made from Geostationary Meteorological Satellite (GMS) infrared data taken from International Satellite Cloud Climatology Project (ISCCP) B3 data sets (see Rossow and Schiffer 1991). The ISCCP data set is comprised of reduced resolution versions of original GMS imagery, with a nominal time and space resolution of 3 h and 30 km. GMS data is gathered eight times per day: at 0030, 0330, 0630, 0930, 1230, 1530, 1830, and 2130 UTC. Reduced resolution of the ISCCP data inevitably smoothed out some fine features, but for purposes of identifying and classifying TCCs by areal extent of cold cloud tops it proved entirely adequate.

The SSM/I sensor aboard the Defense Meteorological Satellite Program F-8 satellite flies at an altitude of 833 km in a near-circular, near-polar, sun-synchronous orbit. Data is gathered at an inclination of 53°. The F-8's equatorial crossing times in the ascending and descending nodes are

0612 LST and 1812 LST, respectively. In the near-equatorial region of this study, actual pass times occurred within 10 minutes of nodal crossing times. SSM/I's narrow swath width of 1394 km leaves substantial gaps in horizontal coverage; successive 12 hourly passes rarely cover the same region. SSM/I gathers microwave data at four frequencies: 19.35 GHz, 22.235 GHz, 37.0 GHz, and 85.5 GHz (hereafter: 19 GHz, 22 GHz, 37 GHz, and 85 GHz). A total of seven channels collect data in the horizontally and vertically polarized planes at 19 GHz, 37 GHz, and 85 GHz, and in the vertically polarized plane only at 22 GHz. Table 1, from Hollinger (1987),

Table 1. Specifications of the F8 SSM/I. Source: Hollinger (1987).

Characteristics	Specifications
Frequencies (GHz)	85.5, 37, 22.235, 19.35
Polarization	H, V (only V at 22.235)
Radiometer type	Total power
Feed-antenna relation	Synchronously rotating
Swath width	1394 km
Scan type	Continuous rotation
Earth incidence	53°
Spatial resolutions (integrated 3 dB limits, km)	16 x 14 @ 85.5 GHz
	38 x 30 @ 37 GHz
	60 x 40 @ 22.235 GHz
	70 x 45 @ 19.35 GHz

presents the specifications of the F8 SSM/I, indicating an increase of spatial resolution with frequency.

SSM/I data for this study were taken from tapes prepared by Remote Sensing Systems (RSS) from original data collected at the Navy's Fleet Numeric Oceanographic Center. RSS data are tabulated in scanlines normal to the satellite path. A scan record includes pixel antenna temperatures for each SSM/I channel, and surface flags for water, coastline, land, vegetation, permanent sea ice, and possible sea ice. Sampling density at 85 GHz is 12.5 km²; at all other channels it is 25 km². For the data set used in this study, antenna temperatures were converted to brightness temperatures (TBs) for all open ocean scan records in the region between 140°E and 170°W and between 20°N and 20°S. To allow multichannel comparisons, the higher sampling density at 85 GHz was averaged to match the sampling density at other channels. In addition, a high-resolution data set was prepared using the full sampling density at 85 GHz.

Twice-daily (0600 and 1800 UTC) streamline and wind vector fields were generated at 850 mb and 200 mb from the European Center for Medium Range Weather Forecasting (ECMWF) data base. Spatial resolution of the ECMWF grid is 1.125° x 1.125°. ECMWF maps were useful in determining the synoptic scale dynamic environment of the TCCs, and in identifying large-scale forcing.

Surface and upper air observations are sparse in the region of this study. The Air Force's Environmental Technical Applications Center provided rawinsonde and surface observations, including precipitation data, from five reporting stations in the region: Andersen AFB, Guam (13.33°N, 144.50°E), Ponape Island (6.58°N, 158.14°E), Truk International/Moen Island (7.27°N, 151.50°E), Majuro/Marshall Island (7.05°N, 171.23°E), and Pago Pago (14.20°S, 170.43°W). Sparse as they were, reports from these stations proved useful in validating algorithms, providing a check on general accuracy of ECMWF wind data, and in establishing tropopause level, freezing level, and other significant features of the tropical atmosphere for the period of this study.

2.2 Methodology

Tropical convection occurs in a large range of spatial and temporal scales, from discrete transient cumulonimbus cells several kilometers in radius to "super clusters" thousands of kilometers in extent and a week or more in duration (Lau and Sui, 1991). Between these extremes, tropical cloud clusters fall in the mesoscale range, roughly 100 km to 500 km in diameter, with a lifetime of 12 to 24 hours (see Houze, 1982). The term TCC, however, is applied loosely in published studies. TCCs have not been accorded a specific, generally accepted definition based on IR satellite

signature, analogous to the quantitative criteria established by Maddox (1980) for the more tightly organized Mesoscale Convective Complexes (MCCs). To the extent that the TCCs are discrete entities, it seems reasonable to begin an empirical study with a statement of minimum thresholds. Accordingly, cloud features, excluding tropical cyclones, had to meet the following criteria to be considered for this study:

- a single continuous cloud shield with an equivalent blackbody temperature $< -65^{\circ}\text{C}$, covering an area of at least 60,000 sq km (length scale of roughly 250 km or 2°)
- maintenance of this cold cloud shield for at least 6 hours

Though somewhat arbitrary, these criteria are physically based and provide a reasonable starting point for identifying TCCs. Mature TCCs were identified by their extensive continuous cloud shields, distinguishing them from both individual cumulonimbus cells, whose anvil clouds are not extensive, and synoptic scale superclusters, whose cloud tops are not continuous. Because the tropopause is extremely high in the tropical western Pacific (roughly 17 km), a cold -65°C threshold temperature was applied--considerably lower than Maddox's -52°C threshold for MCCs. The -65°C IR contour (roughly 14 km in altitude), has been assumed to correspond fairly well to regions of organized precipitation in the tropics (Webster and Houze, 1992). A minimum spatial requirement insures the cluster is of requisite scale to generate a dynamically active stratiform precipitation area. In addition,

clusters had to be large enough to be resolvable at the rather coarse resolution of the SSM/I data. The length scale of 250 km corresponds to Class 3 (and above) convective systems, as defined by Webster and Lucas for TOGA COARE aerial reconnaissance (1992). Because TCCs tend to be more amorphous than mid-latitude MCCs, often lacking the tight centroid that is a defining feature in Maddox's classification, no shape requirement was included. A minimum time criterion was included, although it is probably redundant since mesoscale systems almost invariably last longer than 6 hours.

Because the outward spread of the cloud canopy is fueled by underlying convection and the generation of mesoscale ascent in upper levels, it seems plausible to relate life cycle stage of a cluster to the size of its canopy. It was therefore assumed that the cluster had achieved peak maturity when the continuous cloud shield reached its maximum areal extent. The period before reaching maximum extent was assumed to be the formative phase; after, the dissipating phase. In actual practice this criterion was difficult to apply with great precision. Due to the often slow expansion of the canopies and the crude time resolution of the GMS satellite imagery, it was necessary to interpolate a best guess for time of peak maturity between 3-hourly images, with a possible 1-2 hour error, a method applied to West Pacific MCCs by Miller and Fritsch (1991). In the absence of other

confirming data, life cycle estimates from IR imagery, provided a useful baseline against which to compare SSM/I analyses of the TCCs.

Once TCC cases were identified and stages of development assessed by their IR signature, horizontal fields of various SSM/I-derived parameters were generated. Significant time discontinuities between GMS and F-8--up to one and one-half hours--permitted only general comparisons between GMS IR and SSM/I data. Maps of various SSM/I-derived parameters were prepared, and comparison of these parameters accomplished by means of cross sections. Composite geophysical profiles of TCCs in various stages of development were also prepared.

CHAPTER 3

GEOPHYSICAL PROPERTIES OF MICROWAVE RADIATION

Radiation in the microwave portion of the spectrum (roughly 0.1 cm to 10 cm in wavelength, or 180 GHz to 6 GHz in frequency), has a number of unique properties that can be exploited in the study of precipitating weather systems. Microwave radiance values emerging at the top of the atmosphere and measured by the downward-looking SSM/I vary in consistent ways with geophysical properties of the atmosphere and underlying surface. The purpose of this chapter is to summarize briefly those basic responses of the microwave channels that make retrievals of atmospheric parameters possible.

3.1 Emission by Atmospheric Gases

Microwave radiation is significantly absorbed and emitted by two gaseous constituents of the atmosphere: water vapor and molecular oxygen. Figure 1, a plot of total atmospheric microwave transmittance as it varies with wavelength, depicts the effect of these constituents alone (excluding precipitation and clouds) on microwave radiation. The various SSM/I frequencies are indicated by the broken vertical lines. Molecular oxygen is a strong absorber of microwave radiation, especially in the wavelength interval

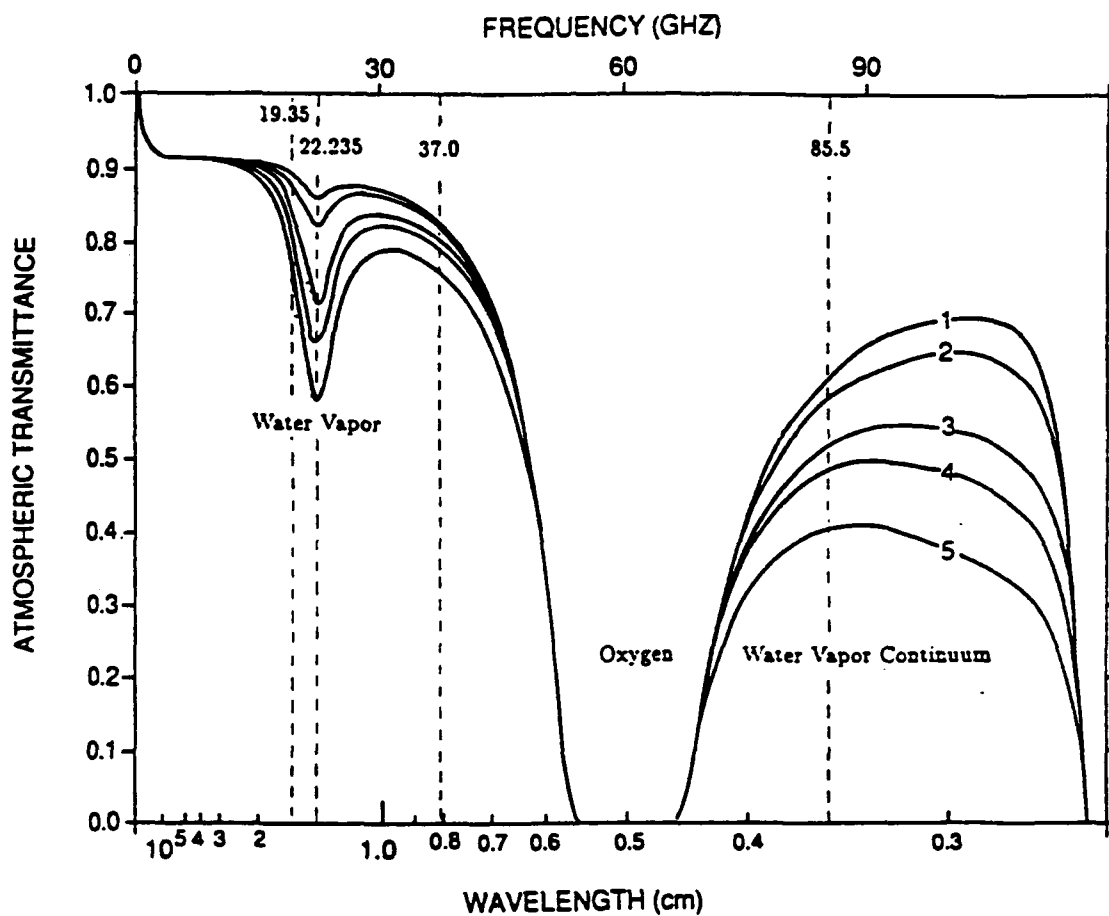


Figure 1. Total atmospheric microwave transmission for a zenith angle of 53°. Model atmospheres used are (1) wintertime polar, (2) summertime polar, (3) wintertime midlatitude, (4) summertime midlatitude, and (5) tropical. Source: Petty (1990).

between 0.65 cm and 0.46 cm, where the atmosphere is virtually opaque. Though weakly dependent on pressure and temperature, the effect of atmospheric oxygen on microwave transmittance is predictable and easily calculated. Atmospheric water vapor, however, is highly variable in space and time, and has a significant bearing on clear sky transmittance in the microwave range. The multiple curves in Figure 1 represent transmittance for various modelled airmasses, from wintertime polar (dry) to tropical (wet). Variations in total atmospheric water vapor obviously affect microwave transmission, especially near the inverted "spike" centered on 22 GHz and in the water vapor continuum portion of the spectrum where the 85 GHz channel is located. This property of water vapor emission is exploited by retrieval algorithms when information about atmospheric water vapor is desired, but must be factored out when other atmospheric parameters are sought.

3.2 Emissions by the Earth's Surface

Besides atmospheric oxygen and water vapor, the earth's surface emits significant microwave radiation. Radiative properties of a flat water surface are derived and explained by Swift (1980). In general, the emissivity of land is higher than that of the ocean. But the radiative properties of land are also more variable, depending on vegetation, snow

cover, soil type, and moisture content. Compared to land, the ocean surface presents a smooth, though "cool", optical surface in the microwave range, with average emissivity in the range 0.4 to 0.5. Microwave emissivity of the ocean surface varies with salinity, temperature, and wind-roughening of the water surface (Wilheit and Chang, 1980). But, in general, these factors are much smaller than the variability inherent in a land surface. Because of its low emissivity, an ocean surface provides a uniform backdrop against which "warm" atmospheric emissions can be distinguished by microwave sensors. By contrast, it is difficult to discriminate between a highly emissive land surface and atmospheric emissions of nearly the same brightness temperature (TB). For these reasons, microwave algorithms based on atmospheric emissions are applied almost exclusively to oceanic regions, as in the case studies chosen for this research project.

From the known optical properties of the ocean surface and of the gaseous atmospheric constituents overlying it, microwave radiance values can be calculated at the top of a clear atmosphere using a plane parallel radiative transfer equation (see Wilheit *et al.*, 1977, for an early theoretical model). The output in Figure 2 shows clear-sky brightness temperatures (TBs) over a smooth ocean of constant temperature for each SSM/I channel as a function of atmospheric water vapor. A number of general conclusions bearing on the retrieval of atmospheric parameters can be gleaned from this

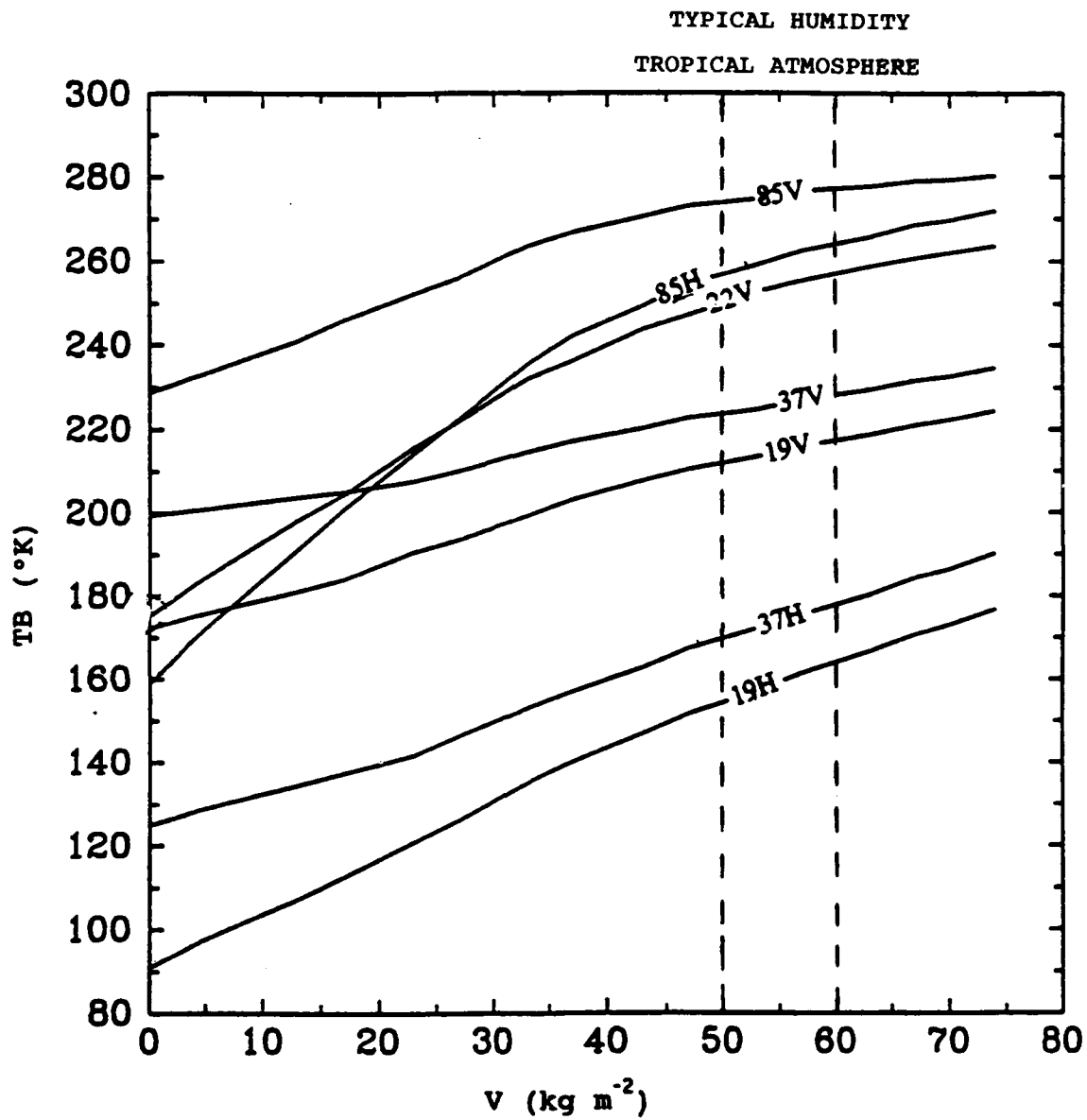


Figure 2. Typical SSM/I brightness temperatures plotted as functions of total atmospheric water vapor V . Atmospheric temperature and other parameters are allowed to vary with V . No cloud water is assumed. Source: Petty (1990).

figure. First, brightness temperature of the ocean surface varies strongly with frequency. With no overlying water vapor, the difference in brightness temperature between 85V (vertically polarized 85 GHz) and 19H (horizontally polarized 19 GHz) is almost 140°K. Secondly, when viewed at an oblique angle the ocean surface is more emissive in the vertically polarized than in the horizontally polarized plane. With the 53° viewing angle of SSM/I, each channel exhibits large polarization over the open ocean. The degree of polarization is wavelength dependent, from a maximum difference of 65°C at 85 GHz to over 80°C at 19 GHz. Third, increases in atmospheric water vapor raise the TBs in all channels, though in varying degrees. Because atmospheric water vapor is a much more effective emitter/absorber of microwave radiation than is a plane water surface, it registers warmer TBs than the underlying ocean, even though it is almost always thermometrically cooler. Finally, increases of brightness temperature with additional water vapor are more pronounced in the horizontal than in the vertical plane of each channel. One important consequence of water vapor's presence in the atmosphere is that it reduces polarization of the open ocean surface, absorbing the polarized upwelling radiation and replacing it with unpolarized emission from the water vapor molecules. Depolarization of surface radiation by atmospheric constituents has profound significance for microwave retrieval algorithms, as will be discussed in Chapter 4.

To test the clear-sky model output against actual data in the western Pacific, a composite cross section from an SSM/I pass over the western Pacific was prepared at 85 GHz, 37 GHz, and 19 GHz, in both horizontal and vertical polarizations (Figure 3). The area of the cross section was determined from satellite pictures to be free of cloud. For integrated water vapor in the range of 50-60 kg/m²--typical of a tropical airmass in the western Pacific--the modelled brightness temperatures (Figure 2) agree reasonably well with clear-sky TBs presented in Figure 3. Small horizontal variations are evident, particularly in the slight "warm" bulge between 178°W and 176°W.

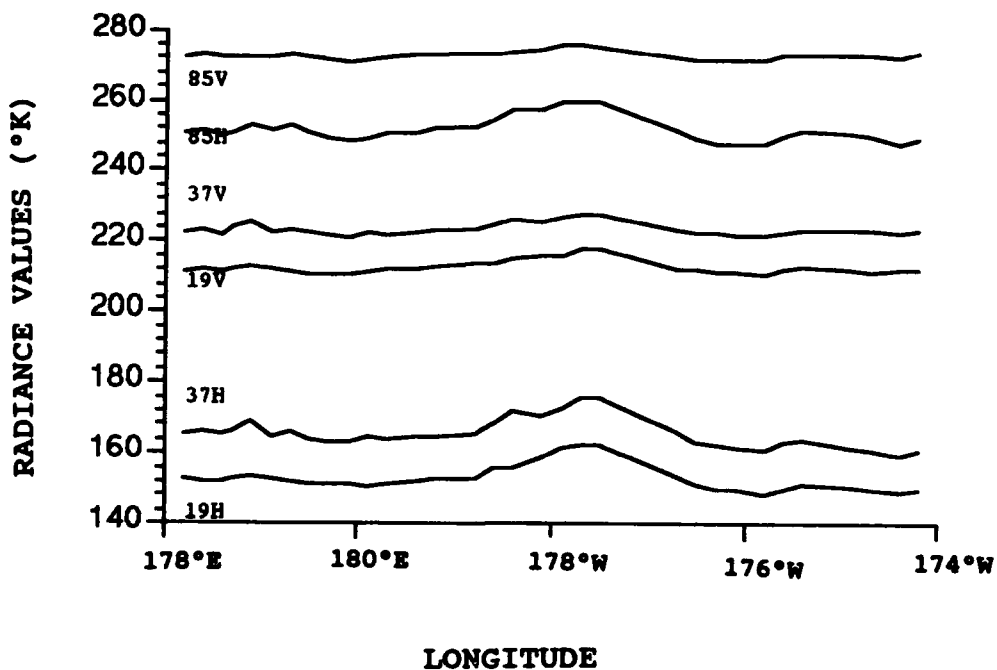


Figure 3. Cross section of SSM/I clear-sky radiance values in western Pacific: 13 November 1987 1927 UTC. Along Equator.

Sea surface temperatures vary little in this region, so the most likely cause of increased TBs is either wind-roughening of the surface or elevated values of integrated water vapor along the path of the cross section. These inhomogeneities are slight, however. In general, the ocean presents a smooth radiative surface, making it a good background for the retrieval of atmospheric parameters by SSM/I.

3.3 Emission and Scattering by Clouds and Hydrometeors

Liquid cloud droplets absorb and emit microwave radiation independently of drop size. As predicted by the radiative models of Wilheit *et al.* (1977), Weinman and Guetter (1977), Huang and Liou (1983), and Spencer *et al.* (1983), intervention of cloud and precipitation over a water surface introduces two complementary effects: an increase in total microwave emission and a lessening of polarization. Figure 4 is a schematic depiction of the effect of cloud water and precipitation on radiance values at 37 GHz. The vertical axis, average brightness temperature (TB AV), depicts the emission effect, while the horizontal axis, the brightness temperature difference between the vertical and horizontal polarizations (Δ TB), measures the polarization effect. From a cool, highly polarized clear-sky value (marked "ocean surface"), increases in cloud liquid water cause reduced polarization and warmer average brightness temperatures along a linear path,

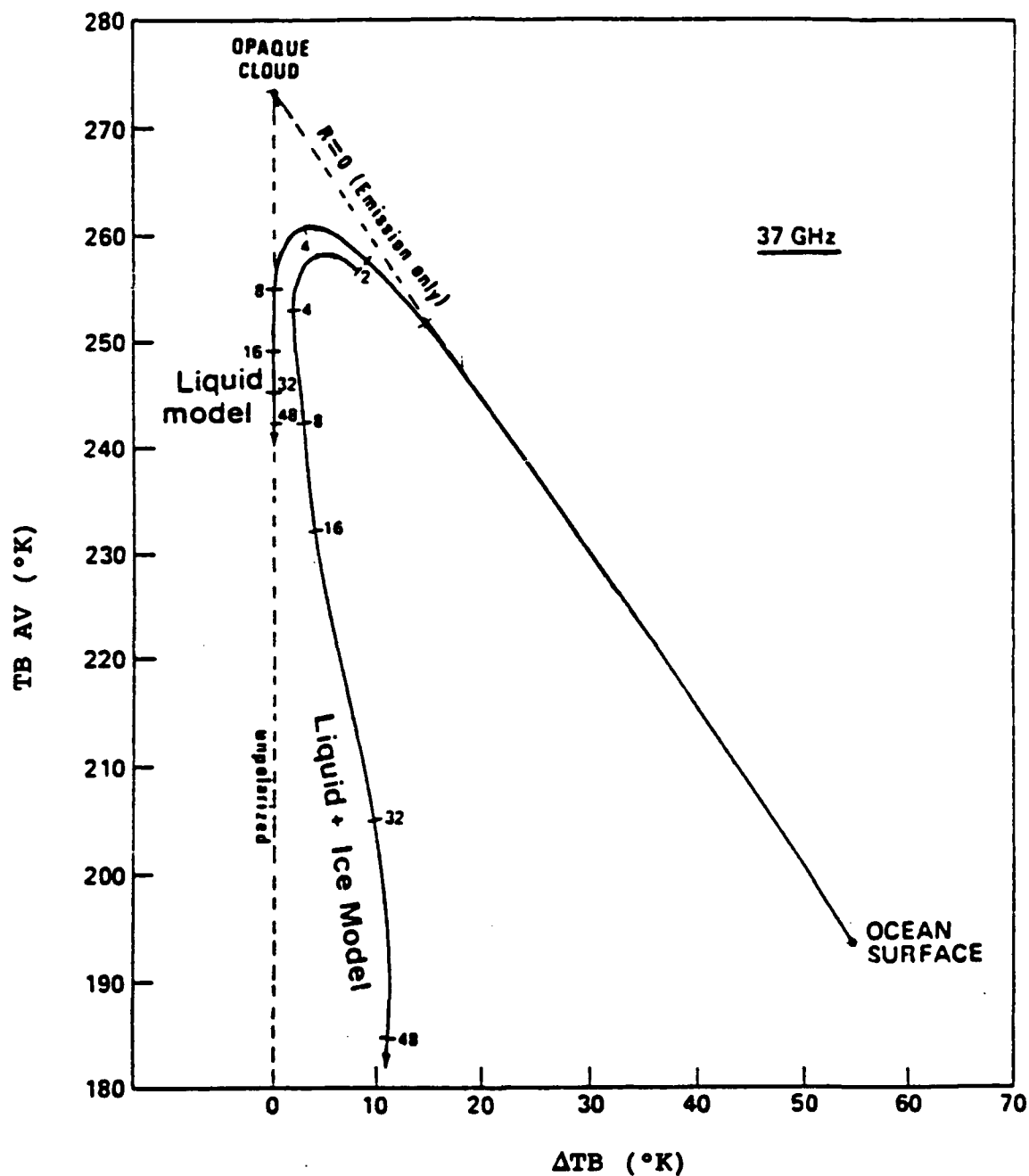


Figure 4. Schematic depiction of how 37 GHz brightness temperatures change with increasing rain rate and/or cloud opacity. Horizontal axis is $\Delta TB = (TBV - TBH)$; vertical axis is $TB AV = (TBV + TBH)/2$. Numbers on curves indicate rainrates in mm/hr. Source: Spencer (1986).

designated on the graph as "emission only", toward higher average brightness temperature and lower polarization. As clouds thicken and atmospheric opacity increases, progressively more of the upwelling surface radiation is attenuated and replaced with "warm" unpolarized radiation. In effect, the elevated TBs are the result of the satellite radiometer "seeing" less of the surface and more of the cloud. The "emission only" path leads, theoretically, to a totally opaque cloud ($\tau \rightarrow \infty$) of zero polarization difference and optimum brightness temperature.

In actuality, the theoretical radiative signature of a totally opaque cloud is approached, but never reached. The reason for deviation from the linear path between clear sky and the totally opaque end point is a complex interaction of radiative processes that commence in optically thick clouds (see Smith *et al.*, 1991, for a very detailed radiative model). As the cloud becomes thicker it increases in opacity and the effective emitting level moves to higher levels in the cloud. Since lapse rates are usually negative, the satellite receives most of the emitted microwave radiation from higher, cooler atmospheric source regions, resulting in depressed TBs.

Even more important than raising the effective emitting level is the effect of scattering on a cloud's microwave signature, as quantified in various modelling studies (Wilheit *et al.*, 1977; Huang and Liou, 1983; Wu and Weinman, 1984; Olson, 1989; Adler *et al.*, 1991; Smith *et al.*, 1991). The radiative theory behind these models can be summarized simply. As

clouds thicken, coalescence processes take over and, at some point, precipitation begins. Droplets growing to precipitation size assume a scattering cross section that is no longer negligible in the microwave range. From Table 2 we see that the transition from a Rayleigh scattering to a Mie scattering regime at microwave frequencies occurs as droplets grow to precipitation size (100 μm to 1000 μm). If the size parameter $2\pi r/\lambda$ (where λ is wavelength of the radiation and r is radius of the scattering particle) exceeds a threshold of around 0.2, upwelling radiation from layers below will be substantially scattered. This results in a detectable depression of brightness temperatures below modelled "emission only" values.

In the schematic diagram for 37 GHz (Figure 4), scattering by raindrops appears as a deflection of the "liquid model" (rain) curve below the linear "emission only" signature of an opaque, but non-raining cloud. At a modelled rainrate of 2 mm/hr, assuming a Marshall-Palmer distribution of raindrops, the liquid rain curve deviates noticeably below the "emission only" line; up to 8 mm/hr the average brightness temperature levels off, then decreases, while the polarization difference drops to zero. At higher rainrates, polarization remains zero, while increased scattering from a deeper layer of hydrometeors depresses the average brightness temperature still further.

From this schematic, it appears that thin non-precipitating clouds and heavy rain clouds may actually radiate at the same average TB, provided the

Table 2. Size parameter of variable-size drops at a range of microwave frequencies. The table is divided into a Rayleigh regime (upper left) and a Mie regime (lower right, italic) using a 0.2 size-parameter threshold. Source: Smith *et al.* (1991).

Frequency (GHz)	Average cloud drop 10 μm	Large cloud drop or small raindrop 100 μm	Average raindrop 1000 μm
5	0.0010	0.010	0.10
10	0.0021	0.021	<i>0.21</i>
20	0.0042	0.042	<i>0.42</i>
35	0.0073	0.073	<i>0.73</i>
85	0.018	0.18	<i>1.8</i>
130	0.027	0.27	<i>2.7</i>
230	0.048	<i>0.48</i>	<i>4.8</i>

scattering is sufficiently large. As pointed out by Weinman and Guetter (1977), polarization resolves the ambiguity: radiation from thinner non-raining clouds is much more polarized than that from heavy rainclouds. This discrimination is crucial in retrieving unambiguous rainfall rates over the ocean.

The case of ice precipitation is quite different from that of exclusively liquid precipitation, requiring a separate modelled curve (see Wu and Weinman, 1984; Spencer, 1986). Because the single scatter albedo of ice approaches unity, frozen hydrometeors scatter more and radiate

proportionately less microwave radiation than do liquid drops of the same size. As a result, the "liquid + ice" modelled curve in Figure 4 indicates far larger depressions of brightness temperature than does the liquid model at the same rainrates. In addition, the "liquid + ice" curve displays a residual polarization difference of over 10°C at higher rainrates. The reason, proposed by Wu and Weinman (1984), and corroborated by Spencer *et al.* (1989), is that ice particles in a precipitating cloud, especially plates and dendrites, fall with a horizontal orientation relative to the ground, thus acting as preferential scatterers in the horizontal plane. In contrast to essentially spherical liquid raindrops, which scatter non-preferentially, precipitating ice particles maintain a residual polarization difference.

It should be noted that the lower part of the "liquid" curve is purely hypothetical and not at all realistic. Rainrates in excess of 20 mm/hr are almost exclusively convective and therefore likely involve an ice phase (Rogers and Yau, 1989). Even in the case of somewhat lighter stratiform rain, there is a great likelihood of significant frozen hydrometeors aloft. Thus, it seems reasonable to expect actual tropical systems to conform more closely to the "liquid + ice" than to the "liquid" model, especially where precipitation is heavy.

3.4 An Example

To test Spencer's modelled radiance values with actual SSM/I data a mature, well-organized tropical cloud cluster from 14 November 1987 was selected for analysis (Figure 5). A scatter plot (Figure 6) made from data in the outlined area of the GMS image displays general similarity to Spencer's model at 37 GHz (Figure 4). Data points outside the periphery of the storm lie along the "emission only" line, from the clear-sky "ocean surface" value,

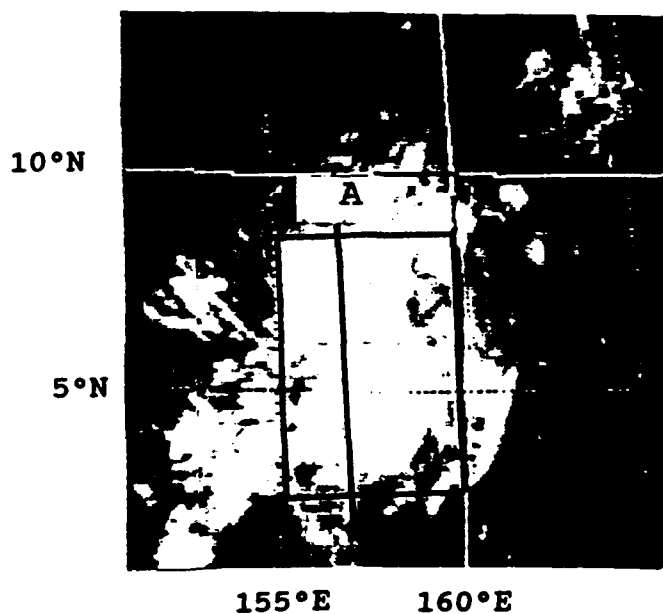


Figure 5. GMS unenhanced IR: 14 November 1987 2130 UTC.

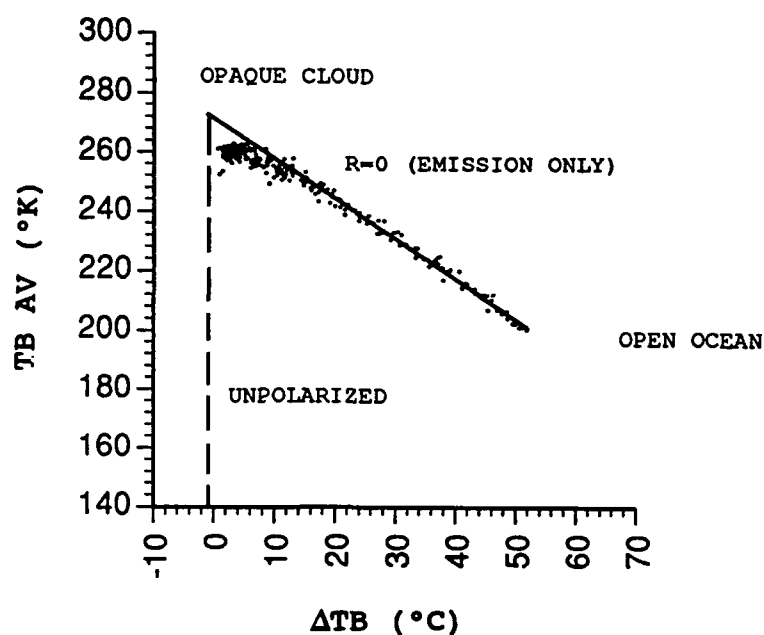


Figure 6. Average brightness temperature and polarization at 37 GHz: 14 November 1987 2056 UTC. From 3°N to 8°N and 155°E to 160°E.

through non-raining clouds of increasing depth and optical thickness. Data points from lightly precipitating regions begin to dip below the "emission only" line at ΔTB of around 20°C, with TBs levelling off and even decreasing slightly in regions of heavier precipitation. Actual brightness temperature depressions, however, are far less pronounced than one would expect from either the liquid or ice modelled curve, especially in such an apparently intense TCC. The "liquid + ice" curve predicts an average TB of

around 230°K for a rainrate of 16 mm/hr, but precipitating areas in the example do not radiate at less than 250°K.

In comparing modelled values to actual data, one must always bear in mind that satellite-based brightness temperatures represent spatially averaged values. For instance, an instantaneous rainrate as high as 50 mm/hr, while not particularly heavy for tropical convection, is almost never encountered over the entire extent of an SSM/I footprint. In the case of some SSM/I channels, the footprint is as large as 40 km x 60 km, or 2400 km². Radiative models, on the other hand, are usually one-dimensional and assume horizontal homogeneity within the grid space. The inherent limitation of SSM/I resolution would explain why scattering-based temperature depressions measured by SSM/I are far smaller than the models suggest. An inverse relationship of spatial scale to rainrate tends to mask the microwave signatures of small intense convective features, and must always be considered when comparing actual microwave data with modelled values. Smoothing, or beamfilling, is a key problem in interpreting microwave analysis of precipitating systems and will be discussed in individual case studies.

Scattering properties of rain clouds, expressed as a function of the size parameter $2\pi r/\lambda$, are highly dependent on wavelength, as is evident from an inspection of Table 2. Plots of 19 GHz and 85 GHz radiance values, made from the same 14 November, 1987, TCC, reveal this wavelength

dependence graphically. At 19 GHz (Figure 7) data points follow an emission line with virtually the same slope as at 37 GHz. Unlike the 37 GHz plot, however, the 19 GHz plot displays no deviation from linearity with increasing cloud thickness and rainrate. From Mie theory, the effective scattering cross section of a hydrometeor is an inverse function of wavelength. Thus, raindrops of a middle size range (around $1000 \mu\text{m}$), which scatter considerable 37 GHz radiation, present a much smaller

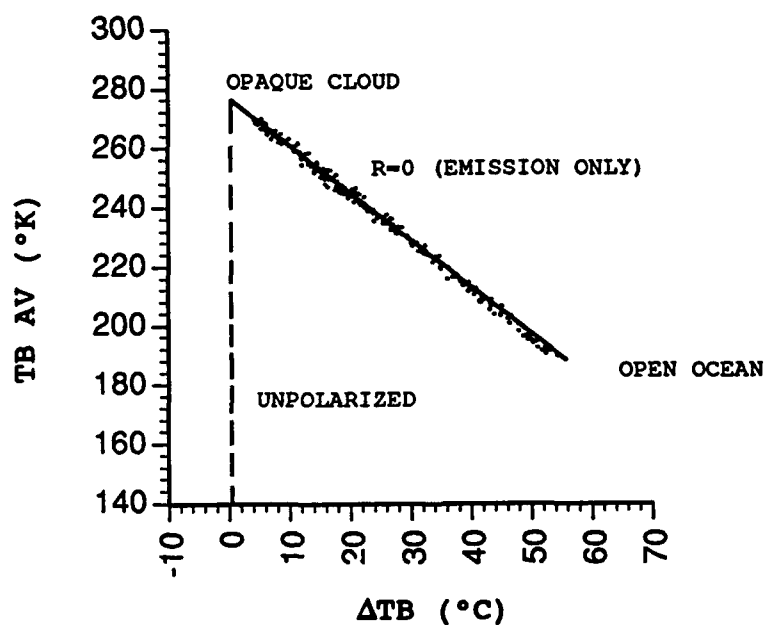


Figure 7. Average brightness temperature and polarization at 19 GHz: 14 November 1987 2056 UTC. From 3°N to 8°N and 155°E to 160°E .

scattering cross section at 19 GHz. Modelling studies by Wilheit *et al.* (1977), and subsequent high-resolution observations (see Adler *et al.*, 1990a) indicate scattering effects become discernible at 19 GHz only at rainrates in excess of 50 mm/hr over the extent of the SSM/I footprint. As a result, scattering by heavy rain and even large graupel in convective cells is usually not detectable at this wavelength. More commonly, heavily raining pixels at 19 GHz tend to saturate at a maximum TB of 265°K for rainrates in excess of 20 mm/hr, without noticeable deviation below the "emission-only" line.

The situation is quite different at 85 GHz (Figure 8). From open ocean through very thin non-precipitating cloud, data points at 85 GHz follow the linear "emission-only" path, increasing in average brightness temperature and decreasing in polarization. In thicker cloud and precipitating regions, however, deviation from the linear "emission-only" path is much more pronounced than in the plot at 37 GHz. At 85 GHz, brightness temperatures fall to more than 100°C below the opaque cloud value. Scattering of upwelling radiation by smaller hydrometeors and even cloud droplets alone is sufficient to drop received radiance values at 85 GHz appreciably below the emission only line. Heavily precipitating data points at 85 GHz are characterized not only by decreasing brightness temperatures, but by discernible increases in residual polarization, up to 8°C. The outline of data points in this portion of the scatter plot is similar to the shape of Wu and

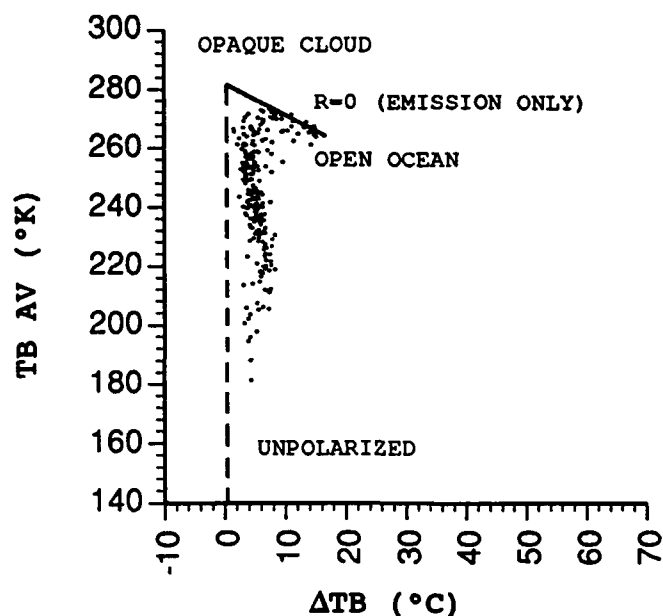


Figure 8. Average brightness temperature and polarization at 85 GHz: 14 November 1987 2056 UTC. From 3°N to 8°N and 155°E to 160°E.

Weinman's modelled "liquid + ice" curve at 37 GHz, but for much lower rainrates.

Variation of rain and ice scattering with wavelength has important consequences for the retrieval of information about weather systems by means of microwave radiation. Because of the wavelength dependence of Mie scattering, different channels "see" into different levels of a precipitating cloud (Wu and Weinman, 1984; Adler *et al.*, 1991; and Smith *et al.*, 1991). Since the 19 GHz channel is impervious to scattering by all but the largest hydrometeors, radiation measured in this channel correlates to rain and cloud water emission integrated through the entire column, but especially below

the freezing level, where most of the liquid water is located. With its acute sensitivity to ice scattering, the 85 GHz channel "sees" only into the top layer of precipitating ice particles, with virtually all the upwelling radiation from the cloud layers below being scattered away. The 37 GHz channel is sensitive to both emission and scattering, depending on the size and number density of hydrometeors. Because radiative properties vary with wavelength, a careful comparison of microwave signatures in multiple channels can reveal something of the gross vertical structure of a tropical cloud cluster--information that could not be derived from any single channel alone.

To illustrate the response of various SSM/I channels to geophysical variations within a tropical cloud cluster, cross sections at three different channels were made through the 14 November cluster. The cross section (marked line "A" in Figure 5) cuts through the brightest convective portion of the cluster. In Figure 9, 19 GHz brightness temperatures in both polarizations are plotted. Between 1°N and 3°N TBs increase gradually from their minimum open-ocean values, the slight warming due to emission from non-precipitating cloud. North of 3.5°N TBs increase abruptly and polarization decreases in response to emissions from precipitating cloud. At 4.5°N, correlated with the surface rainfall peak of 18 mm/hr, 19V reaches its maximum "saturation" value of 265°K and polarization drops to a minimum of 5°C. Between 5°N and 6.5°N emissions taper off in response

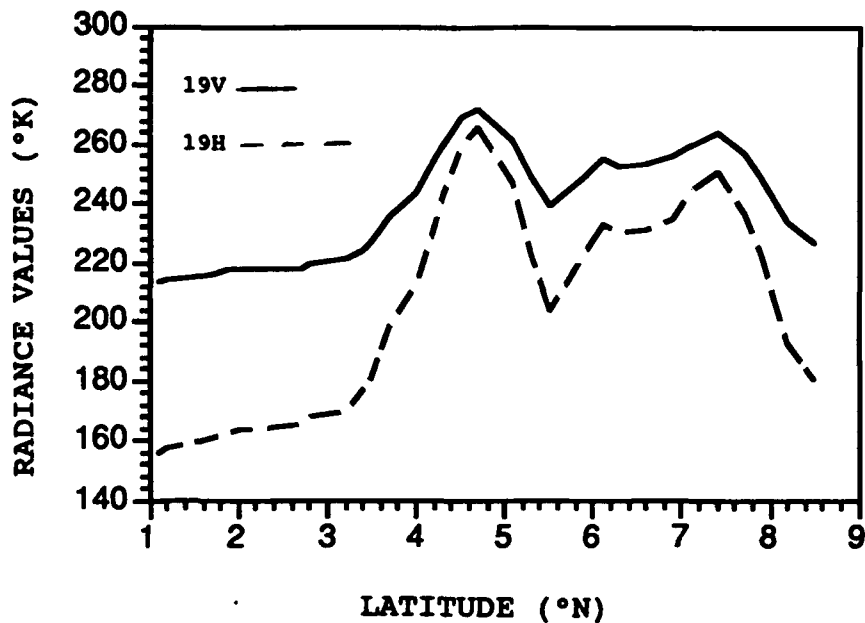


Figure 9. Cross section of radiance values at 19H and 19V: 14 November 1987 2056 UTC Along 157°E.

to the thinner non-precipitating cloud, then gradually increase to another local maximum near 7.5°N as rainfall increases to over 10 mm/hr. North of 8°N, beyond the second rainfall maximum, radiance values drop off, again approaching their clear sky minima.

A cross section through the same region at 37 GHz (Figure 10) exhibits a profile broadly similar to the one at 19 GHz. Markedly higher brightness temperatures and small residual polarizations clearly demarcate

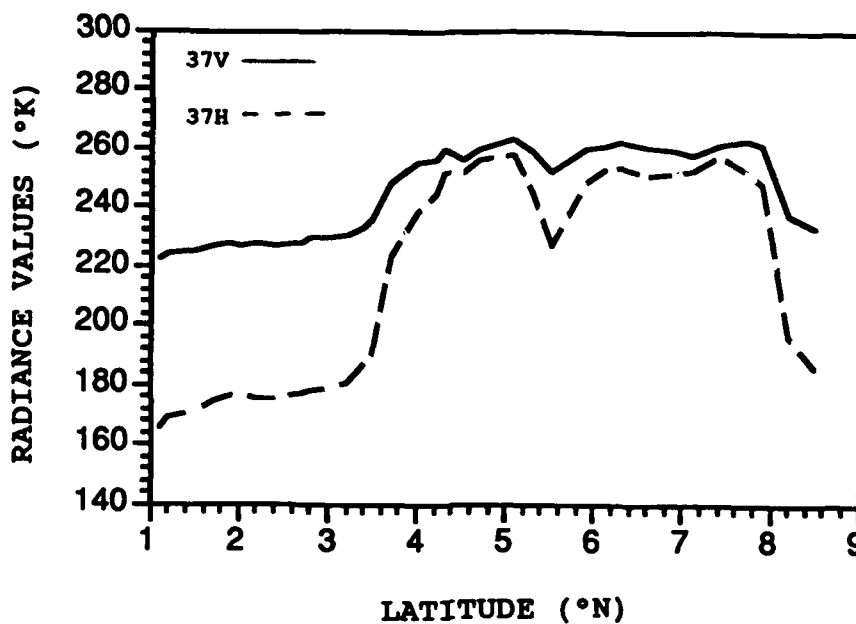


Figure 10. Cross section of radiance values at 37H and 37V: 14 November 1987 2056 UTC. Along 157°E.

the precipitating region between 4°N and 8°N from non-raining regions to the north and south. The two of precipitation peaks, apparent as emission maxima in the 19 GHz profile, are smoothed out at 37 GHz into a single broad emission plateau, with only a small dip in TBs indicating the local rainfall minimum at 5.5°N. A significant exception is the small "notch" in the 37V brightness temperature profile located at 4.5°N, directly over a local rainfall maximum. This slight decrease in TB, unlike the deeper depression at 5.5°N, is most likely due to scattering by large ice particles such as hail

and graupel in a region of especially heavy convective precipitation. Another smaller rainfall maximum centered at 7.5°N registers no such comparable depression.

Scattering effects of precipitation are much more pronounced in the cross section at 85 GHz (Figure 11). Coincident with a rainfall maximum at 4.5°N , TBs drop steeply to near 200°K , well below open ocean values. A second rainfall maximum, centered at 7.5°N , is similarly demarcated by a drop in brightness temperature, to around 220°K . Between 6°N and 7°N , the moderately depressed radiance values (about 240°K) most likely

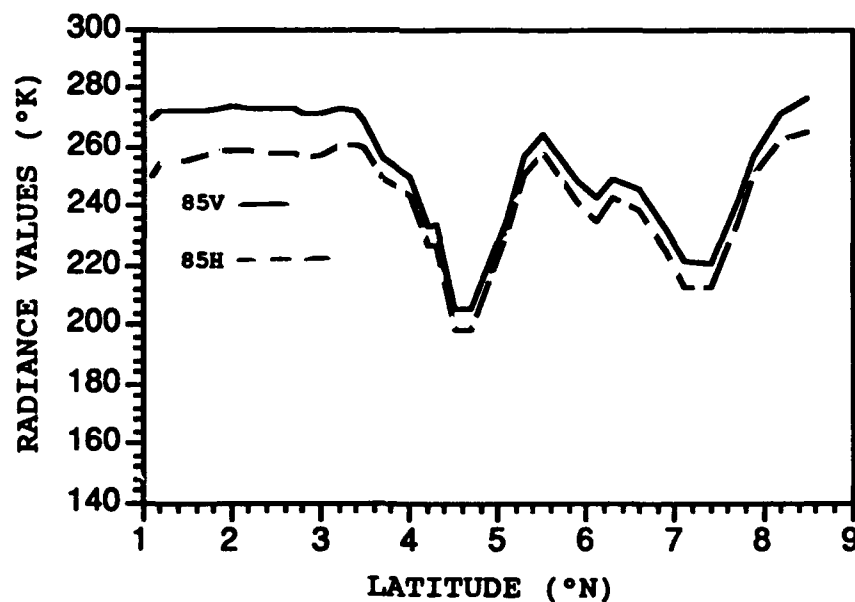


Figure 11. Cross section of radiance values of 85H and 85V: 14 November 1987 2056 UTC. Along 157°E .

correspond to a region of lighter stratiform rainfall. Comparing the 85 GHz cross section with those at 37 GHz and 19 GHz reveals some unique responses of the higher frequency channel. The "notch" at 37 GHz, which merely hinted at scattering by large frozen hydrometeors, is much enlarged at 85 GHz. This is due to the sensitivity to scattering effects at the higher frequency. The two scattering minima at 85 GHz correspond almost exactly to local emission maxima at 19 GHz. This close correlation indicates liquid water emission in the lower levels coincident with ice scattering aloft.

The cross section in Figure 11 was made from a 85 GHz data set reduced to a resolution comparable with the other channels. A full-resolution 85 GHz cross section (Figure 12) reveals the profound effect of beamfilling in masking smaller scale convection. The temperature depression centered at 4.5°N appears nearly 30°C deeper in the high-resolution cross section (170°K versus 200°K), while to the north, in the predominantly stratiform region between 6°N and 8°N, brightness temperatures remain around 215-218°K at either resolution. This variable response of brightness temperature to changes in the resolution of the data can only be attributed to horizontal smoothing of non-uniform precipitation features. Because convective rainfall is inherently small scale and non-uniform, while stratiform rain tends to be horizontally uniform, beamfilling distorts the radiative signature of convective cells far more than it does signatures of stratiform rain. This inherent bias in the SSM/I must be

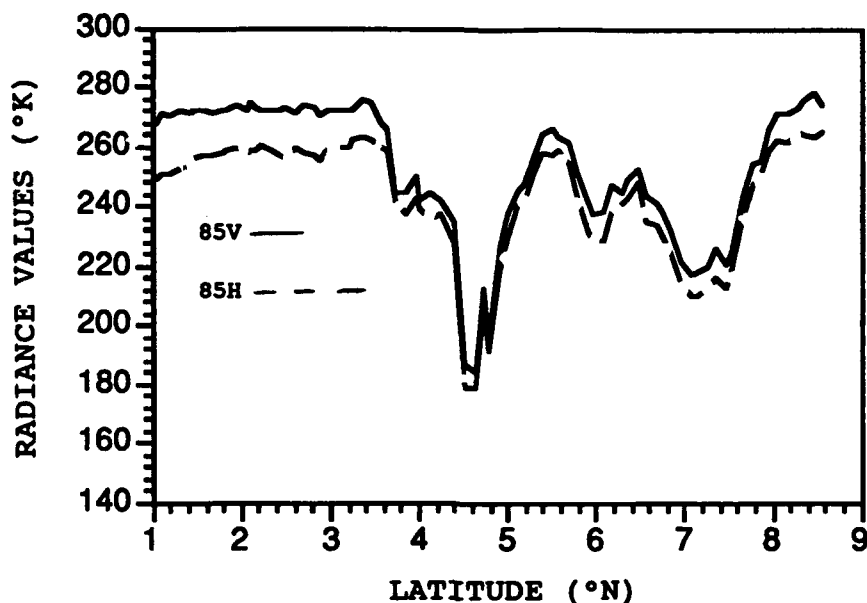


Figure 12. Cross section of radiance values at 85H and 85V (high resolution): 14 November 1987 2056 UTC. Along 157°E.

considered when drawing conclusions about the extent and intensity of convection in TCCs.

In summary, the geophysical properties of microwave channels discussed in this chapter are the basis upon which all SSM/I algorithms for the retrieval of atmospheric parameters are constructed. Key to any retrieval algorithm is the capability to distinguish atmospheric from surface radiation. The radiative contribution of the ocean surface can be factored out, allowing the unambiguous extraction of information about atmospheric constituents of interest (in particular water vapor, cloud water, and hydrometeors). In

addition, the strong frequency dependence of microwave scattering permits vertical profiling. Over precipitating clouds, a satellite radiometer measures emerging TBs from progressively higher layers in the cloud at each higher frequency. As will be shown in case studies, multichannel comparisons permit characterization of the prevailing microphysics of a tropical cloud cluster, as well as assessment of its intensity and life cycle stage.

CHAPTER 4

ALGORITHMS FOR RETRIEVAL OF ATMOSPHERIC PARAMETERS

The algorithms used in this study to retrieve atmospheric parameters all derive validity from the physical response of individual SSM/I channels to emission/absorption and scattering by the atmosphere, as discussed in the Chapter 3. For the purposes of this study, absolute values of retrieved parameters are of less interest than their consistent horizontal variation. Rather than assessing quantitative values, the intent is to analyze fields of retrieved atmospheric parameters qualitatively in order to establish gradients and microphysical profiles of particular cloud clusters. The following chapter consists of brief descriptions of each algorithm used in the case studies.

4.1 Column Integrated Water Vapor

Column integrated water vapor V , also known as precipitable water, is a useful parameter in the study of tropical cloud complexes, particularly their pre- and post-storm environments. It is now understood that V is closely correlated to surface layer specific humidity (Liu *et al.*, 1991; Liu *et al.*, 1992). Sea surface temperature strongly affects the temperature of the boundary layer, resulting in higher water vapor content in the lower layers where the preponderance of V occurs (see Stephens, 1990). The dynamic state of the atmosphere, specifically large scale subsidence and ascent, is

also a strong determinant of the amount of water vapor in an atmospheric column (Prabhakara *et al.*, 1982; Chang *et al.*, 1984). Since sea surface temperatures in the area of this study show little spatial or temporal variation, it is assumed that instantaneous gradients of water vapor in the tropical western Pacific are the result of transport processes and cloud microphysical processes.

Retrieval of water vapor from SSM/I data is made possible by the unique spectral characteristics of water vapor in the microwave wavelengths, in particular the narrow absorption band centered at 22 GHz (see Figure 1). Since the 22 GHz channel is located at the center of the resonant band and the 19 GHz channel is located on the wing, atmospheric opacity due to water vapor alone is quite different for the two channels, while their response to other atmospheric parameters is almost identical. The difference in radiance values at 19 GHz and 22 GHz is thus proportional to the amount of water vapor in a column, and can be regressed to yield an unambiguous value of V which is largely independent of other geophysical parameters (notably, liquid cloud water, sea surface temperature, wind roughening of sea surface).

The multichannel algorithm selected for this study, developed by Bates (1991) from initial work by Alishouse (1989), takes the following form:

$$\begin{aligned}
 V(\text{kg/m}^2) = & 575.66 - 0.403177 * \text{TB19V} - 4.394793 * \text{TB22V} \\
 & + 0.0117982 * \text{TB22V}^2 - 0.356726 * \text{TB37V}. \quad (4.1)
 \end{aligned}$$

The Bates/Alishouse regression-based algorithm was developed by relating V derived from tropical island soundings to collocated SSM/I brightness temperature data.

The advantages of the SSM/I algorithm over water vapor retrieval in the IR $6\mu\text{m}$ window is its greater transparency to clouds. However, it can only be applied to ocean regions, since land applications introduce unacceptably large variations of surface emissivity. Also, the algorithm has been shown to have little reliability in moderate to heavy precipitation. To avoid dubious retrieved values, all rain-contaminated pixels will be flagged using a polarization threshold of $\text{TB19V} - \text{TB19H} < 24^\circ\text{C}$.

For verification, water vapor computed from nearby (within 50 km) rawinsonde stations were compared with SSM/I-derived values. Computations of water vapor from rawinsonde data employed stepwise numerical integration at all significant levels. Results of 36 comparisons are shown in Figure 13. Agreement is generally good in the consistently moist tropical environment though the algorithm underestimates in cases of high humidity. Variation does not necessarily indicate deficiency in the retrieval algorithm, since time mismatches of 3 to 6 hours, and the high variability of water vapor may well have introduced noise into the results. General agreement inspires some confidence in the algorithm.

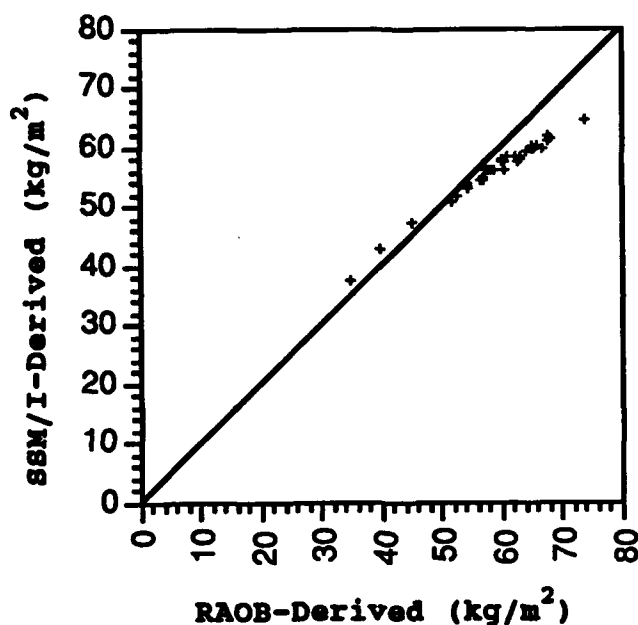


Figure 13. Comparison of SSM/I-derived with RAOB-derived values of integrated water vapor V.

Determinations of water vapor will be key in assessing the pre- and post-storm environments of tropical convective clusters. The correlation between TCCs and elevated values of relative humidity, especially in mid-tropospheric layers, has been documented by Ruprecht and Gray (1976) with widely dispersed rawinsonde data. Ruprecht and Gray's findings will be tested with retrieved field of integrated water vapor around west Pacific TCCs.

4.2 Normalized Polarization at 37 GHz

As shown in Chapter 3, decreased polarization is one of the defining signatures of cloud water and precipitation over the ocean. This general observation prompted Spencer *et al.* (1983) to propose normalized polarization at 37 GHz (P37) as a useful measure of cloud opacity:

$$P37 = \Delta TB37(OBS)/\Delta TB37(CLR) \quad (4.2)$$

where $\Delta TB37(OBS)$ is the observed polarization difference at 37 GHz and $\Delta TB37(CLR)$ is the polarization difference of the cloud-free ocean, which is assumed to remain fairly constant over large areas. P37 equals 1 for clear sky and approaches zero for a totally opaque cloud. Normalization smooths radiative wrinkles in the ocean background, minimizing any unrelated geophysical effects that depress the open ocean polarization below its optimum value. As we have seen, the two primary determinants of clear-sky polarization are atmospheric water vapor and wind roughening of the ocean surface. In the absence of actual surface data to account for these variations, other SSM/I-derived parameters are used to factor out unrelated geophysical effects, as in Petty's (1990) easily-computed form of the P37 ratio:

$$P37 = (TB37V - TB37H) * \exp(0.0151U + 0.00607 * V - 4.4) \quad (4.3)$$

where V is the SSM/I-derived integrated water vapor (see Section 4.1) and U is the surface wind speed (in m/s) derived by the equation

$$U = 1.0969*TB19V - 0.4555*TB22V \\ - 1.76*TB37V + 0.786*TB37H + 147.9 \quad (4.4)$$

Goodberlet *et al.* (1989), in validation studies using buoy data, show that this algorithm for retrieval of wind speed gives reasonable results. Increases in cloud opacity have been shown by Petty and Katsaros (1989) to correlate well to the onset of precipitation. They propose using $P37 < 0.8$ as a fairly reliable indicator of precipitation. Because polarization difference tends to reach a minimum non-zero value in moderate rain, the usefulness of P37 as an indicator of precipitation intensity is limited.

4.3 Liquid Water Path

Liquid water path LWP, defined as the integrated mass of cloud water and rain in an atmospheric column (in units of g/m^2), is a useful but extremely difficult parameter to measure directly. Because LWP is related to cloud optical thickness in the microwave range, it is retrievable from SSM/I data. As shown in the profiles in Chapter 3, brightness temperature varies with cloud water and rain, following an "emission-only" line up to a saturation point. At the same time, the lower frequencies were shown to be insensitive to scattering by all but the largest ice particles. Wilheit and Chang (1980) and Prabhakara *et al.* (1983) demonstrated the feasibility

of deriving LWP from microwave measurements. A different approach, relating LWP directly to atmospheric attenuation as measured by the P37 parameter, was proposed by Petty (1990).

A basic limitation to satellite-based retrievals of LWP is the non-linearity of emission from thick, precipitating clouds, especially at the higher microwave frequencies. Because of this inherent non-linearity, retrieval of LWP is least reliable for thick rain clouds, where results would be most useful in understanding the microphysics of precipitation. To circumvent this serious limitation, Liu and Curry (1992b) have developed a multichannel algorithm to calculate LWP separately for precipitating and non-precipitating regimes. For a non-precipitating regime (determined by $P37 > 0.8$), Liu and Curry, following Takeda and Liu (1987), first calculate cloud emissivity ϵ from the equation

$$A\epsilon^2 + B\epsilon + C = 0 \quad (4.5)$$

where

$$A = aT_c$$

$$B = TB_0 - (1 - a)T_c$$

$$C = TB - TB_0$$

$$a = (1 - TB_0/2)[(1/T_a) + (1/T_s)].$$

T_a , T_s , and T_c are, respectively, mean atmospheric temperature, sea surface temperature, and cloud mean temperature. In the absence of collocated soundings, these values must be derived indirectly. Mean cloud temperature

T_c is derived by a regression equation, using SSM/I data and IR cloud top temperatures from ISCCP data. Clear-sky brightness temperature T_{B_c} is determined from a monthly mean within a $5^\circ \times 5^\circ$ box which is the average of those clear-sky brightness temperatures of nonprecipitating clouds just next to the precipitation threshold. LWP is then calculated for each channel by the following equation:

$$\text{LWP} = (1/\Omega) * \log[1/(1 - \epsilon)] * \cos\theta \quad (4.6)$$

where Ω is the liquid water absorptivity (a function of frequency and mean cloud temperature) and θ is the incident angle (for SSM/I, 53°). In a thin, non-precipitating cloud, the relationship between LWP and TB is nearly linear for all channels. Liu and Curry found the best correlation to the 37H channel; so, for non-precipitating regimes

$$\text{LWP} = \text{LWP}_{37H} \quad (4.7)$$

While all SSM/I channels reach saturation of TB for sufficiently deep clouds, the lower frequency channels are less affected by scattering from large precipitation-size drops. Different saturation limits for 19 GHz and 37 GHz channels suggest that a combination of the two channels would increase accuracy of retrieved LWP in highly opaque precipitating clouds. Accordingly, Liu and Curry propose a linear combination of different channels to retrieve LWP in a rain cloud:

$$\text{LWP} = 0.4 * \text{LWP}_{19H} + 0.6 * \text{LWP}_{37H} \quad (4.8)$$

This dual-channel retrieval in cases of precipitation mitigates LWP underestimates due to scattering. It also compensates for beamfilling in the inhomogeneous rain field.

Because LWP is not routinely measured, validation of the Liu/Curry algorithm is problematic. Their comparison of retrieved LWP with ISCCP data indicates that clear-sky pixels correspond well with retrieved LWP of 0 g/m^2 , while cloudy pixels correspond closely with nonzero LWP. They further find that onset of precipitation is correlated to threshold values of LWP in various regions. In the absence of *in situ* measurements of LWP, these results indicate that the algorithm gives reasonable values as compared to observable cloud properties.

Retrieved fields of LWP will be used in this study to infer the microphysical profile of TCCs, in particular the relative amount of liquid water to frozen hydrometeors in tropical convection.

4.4 Polarization Corrected Temperature at 85 GHz

To exploit the well-documented ice sensitivity of the 85 GHz channel, Spencer *et al.* (1989) proposed polarization corrected temperature at 85 GHz (PCT) as a useful measure of scattering by large frozen hydrometeors. PCT, combining both polarizations at 85 GHz into a single value, has been shown

to be well correlated to the size distribution and depth of the ice layer in a precipitating cold cloud. Spencer defines PCT as follows:

$$\text{PCT} = (\beta \text{TB85H} - \text{TB85V}) / (\beta - 1) \quad (4.9)$$

where

$$\beta = (\text{TB85V}_c - \text{TB85V}_o) / (\text{TB85H}_c - \text{TB85H}_o)$$

The c subscript denotes the brightness temperature for the unobscured ocean surface, and the o subscript denotes the brightness temperature of the ocean surface with no intervening atmospheric layer. In effect, β is the ratio of warming due to atmospheric gases (O_2 , water vapor) in the vertical plane to warming in the horizontal plane. In practical application, β need not be calculated separately for each case, but may be assumed to be a constant within a climatological region. The constant β chosen for this study, 0.45, produced clear sky PCTs that showed remarkably little variation over the tropical western Pacific: 288-291°K, generally. Once computed, the PCT of the unobscured ocean represents a baseline against which to compare scattering depression induced by large particles of hard ice. Spencer has proposed a PCT of < 250°K as a useful threshold for rainfall reaching the surface.

PCT will be used in this study as a means of identifying convective cells beneath the obscuring cirrus canopy of TCCs. As shown by Weng and Vonder Haar (1991), sharp gradients of PCT demarcate convective cells from surrounding stratiform precipitation within tropical systems. Because

PCT responds to microphysical changes near the top of the cloud, it provides a useful contrast to emission-based algorithms, which register, for the most part, processes below the freezing level. Also, with its higher spatial resolution, the 85 GHz channel is better suited to the study of small-scale convective features. As will be demonstrated in the case studies, a simple comparison of PCT to TB19H radiance values throughout a TCC reveals, in broad outline, the dominant microphysical processes within the cluster.

4.5 Ice Water Path

A more physically meaningful parameter than PCT is ice water path IWP, defined as the total mass of frozen water in an atmospheric column. In units of g/m^2 , IWP is conceptually comparable to LWP. Liu *et al.* (1993) have proposed a simple regression of PCT values to yield IWP:

$$\begin{aligned} \text{IWP} &= 8696.0 - 34.8 * \text{PCT} && \text{if PCT} < 250^\circ\text{K} \\ \text{IWP} &= 0 && \text{if PCT} \geq 250^\circ\text{K} \end{aligned} \quad (4.10)$$

In fact, IWP derived by this method is an underestimate. Cloud ice (cirrus) scatters little or no radiation at 85 GHz and is therefore not included in the total derived IWP. In addition, "hard" ice particles (graupel and hail) scatter microwave radiation much more effectively than do "soft" snowflakes of the same dimension, so that the algorithm shows a bias in convective versus

stratiform regimes. Despite these qualifications, derived values of IWP will be useful in assessing the overall microphysics of TCCs, especially in comparison with LWP.

4.6 Rainfall

Algorithms for the retrieval of surface rainrate RR from microwave data may be broadly categorized as emission-based, scattering-based, or attenuation-based. Emission-based algorithms (e.g., Wilheit and Chang, 1980) derive their validity from the observation that raining clouds emit proportionally more radiation than does the cloud-free ocean or atmosphere. Retrieving rainfall amounts is then a matter of tuning a linear relationship between increasing brightness temperatures (especially in the lower frequency channels) and rainfall rates. In scattering-based algorithms it is implicitly assumed that heavier rainfall rates are associated with larger ice particles aloft, which will scatter substantial radiation in the higher frequencies. Spencer (1986) first proposed rainfall retrieval based on scattering in the 37 GHz channel and later proposed a method based on 85 GHz SSM/I data (1989). Petty and Katsaros (1989) have proposed an attenuation-based algorithm which derives rainfall rates correlated to decreasing polarization at 37 GHz in an increasingly opaque raincloud.

Each approach has inherent limitations (see Wilheit, 1986, for a comprehensive overview). Emission-based and attenuation-based algorithms are highly sensitive to light rain, but tend to saturate at precipitation rates between 10 mm/hr and 20 mm/hr, yielding gross underestimates in heavy convective showers. Emission-based algorithms also show substantial sensitivity to variations in freezing level. Scattering-based algorithms, on the other hand, are insensitive to light rain, especially "warm" rain without a scattering ice layer aloft. As a result, they are best used in convection, but have little utility in light stratiform rain.

Liu and Curry (1992a) have proposed a combined emission-scattering rainfall algorithm that mitigates some of the non-linearities of microwave response, making it useful in a wide range of rainfall regimes. By combining the 19 GHz channel, which is sensitive primarily to liquid water emission, and the 85 GHz channel, which is most sensitive to frozen hydrometeors, the Liu/Curry algorithm yields reliable rainrates up to 50 mm/hr. Brightness temperatures in raining pixels are normalized against a baseline value T_{B_0} , representing the brightness temperature of a cloud just before the onset of precipitation. Values of T_{B_0} are determined for 19H and 85H from a radiative cloud model using regional mean values as model parameter inputs. Differences between observed radiance values and the non-precipitating baseline are then determined, and a rainfall rate is calculated from following equation:

$$RR \text{ (mm/hr)} = 0.0055 * (\delta 19H - \delta 85H)^{1.6} \quad (4.11)$$

where

$$\delta 19H = TB19H - TB19H_0 \text{ and } \delta 85H = TB85H - TB85H_0.$$

Because the baseline value TB_0 represents the radiative total of all geophysical processes other than rain, the difference between observed TB and TB_0 is assumed to represent the radiative contribution of rain alone. In this way, extraneous geophysical effects are filtered out of the retrieval.

In this study, the Liu/Curry rainfall algorithm will be used to determine horizontal extent of surface precipitation and its relationship to cold cloud tops in the IR.

CHAPTER 5

CASE STUDIES

From the 15 tropical cloud clusters identified during the period October to November 1987, three have been selected for detailed analysis in this chapter. The intent is to show representative examples of TCCs in each phase of development: formative, intensifying, mature, and dissipating. By a fortuitous circumstance, the cluster from 13 November 1987 is substantially covered by successive SSM/I swaths 12 hours apart, thus providing a rare opportunity to observe the same TCC in different phases of its life cycle with microwave imagery.

5.1 TCC of 13 November 1987--Formative and Mature Phases

From 0600 UTC to 2100 UTC on 13 November 1987 a large, intense TCC developed in the western Pacific between 162°E, 178°E, 2°S, and 7°S. It initially appeared as a random ensemble of discrete cumulonimbus cells (CBs), identified by their cold IR temperatures in GMS imagery (see Figure 14a for contours of equivalent blackbody temperature from 0630 UTC). Over the next 6 hours, the initial group of CBs generated a large (> 100,000 sq km) continuous cloud shield (Figure 14b). By 1530 UTC the < -65°C cloud shield had expanded to over 200,000 km² (Figure 14c) with interior cloud top temperatures of < -75°C over a wide region. GMS

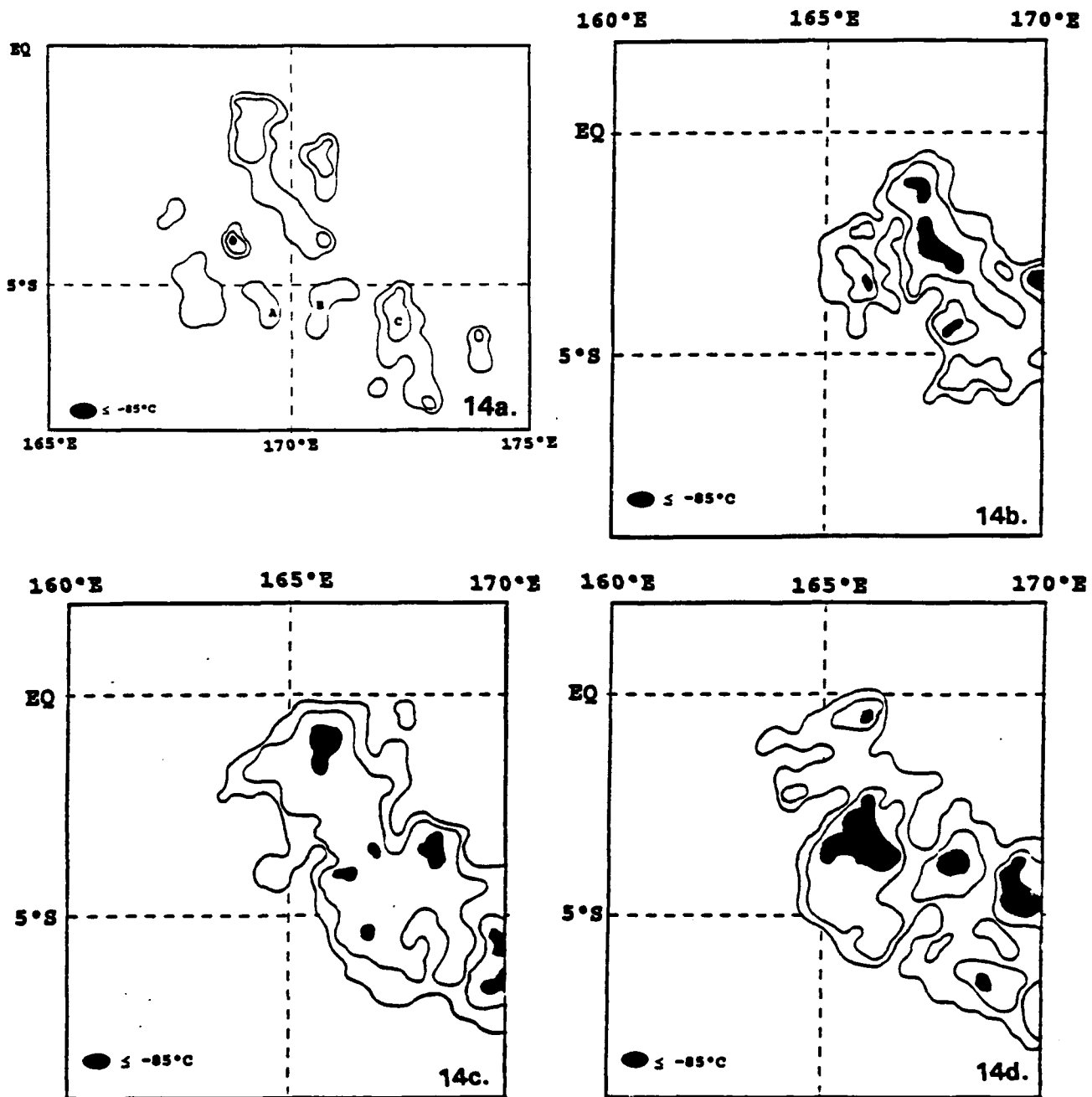


Figure 14a-d. GMS IR Temperatures: 13 November 1987. Contours for -65°C, -75°C, and -85°C. (a) 0630 UTC (b) 1230 UTC (c) 1530 UTC (d) 1830 UTC.

data from 1830 UTC (Figure 14d) reveal that interior cloud top temperatures grew even colder, with extensive areas radiating at blackbody temperatures $< -85^{\circ}\text{C}$. Subsequently, the system's cloud top temperatures increased steadily as the cirrus canopy eroded, indicative of a dissipating storm. Finally, between 2100 UTC and 0000 UTC the continuous cold cloud shield disappeared altogether. Based on IR signatures, peak maturity of the TCC was assigned to 1730 UTC.

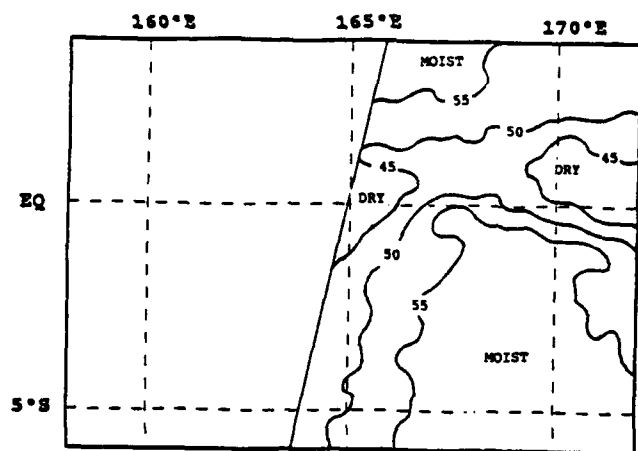
The 13 November TCC developed in the open ocean, far from any large land masses which might have hastened its growth by topographic effects. ECMWF 850 mb streamline analysis from 13 November 1987 1800 UTC (not shown) indicates a weak wave, just upstream from the area of the disturbance. Aloft, anticyclonic flow extending from a closed circulation to the NW was present over the area of TCC development. Coupled with convergence from the wave below, upper tropospheric divergence from the 200 mb anticyclonic flow probably enhanced vertical motions and promoted the cluster's rapid development. ECMWF analyses are useful only to indicate conditions generally favorable to convection. Features of a scale smaller than those resolvable by ECMWF analyses were, in all likelihood, responsible for triggering initial convection from which the TCC eventually developed.

The F-8 pass of 0648 UTC captured the 13 November TCC in its formative phase. At this point the cluster consisted solely of discrete

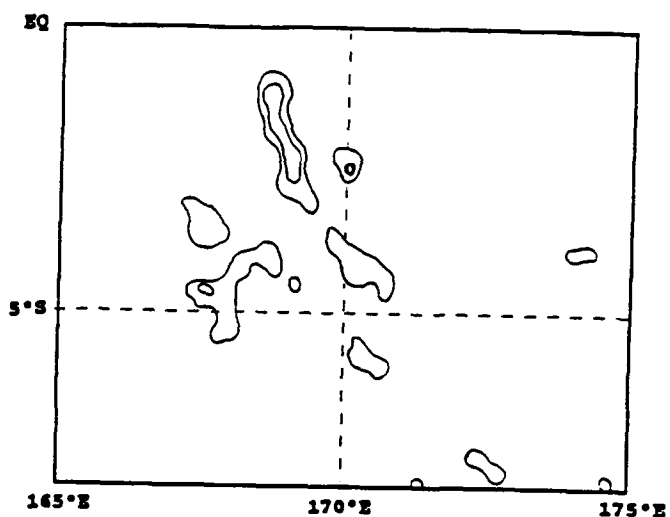
cumulonimbus cells and had not yet generated the characteristic mesoscale cloud shield. SSM/I-derived fields of integrated water vapor V, liquid water path LWP, and ice water path IWP are shown in Figures 15a-d.

The field of integrated water vapor V (Figure 15a) indicates high values, in excess of 55 kg/m^2 , throughout the environment of the initial CB cluster. A distinct moisture maximum appears between 166°E and 172°E , set off by a relatively dry region to the north and west. It is presumed that the unusually moist environment resulting from gentle, large-scale ascent provided conditions favorable to convective development.

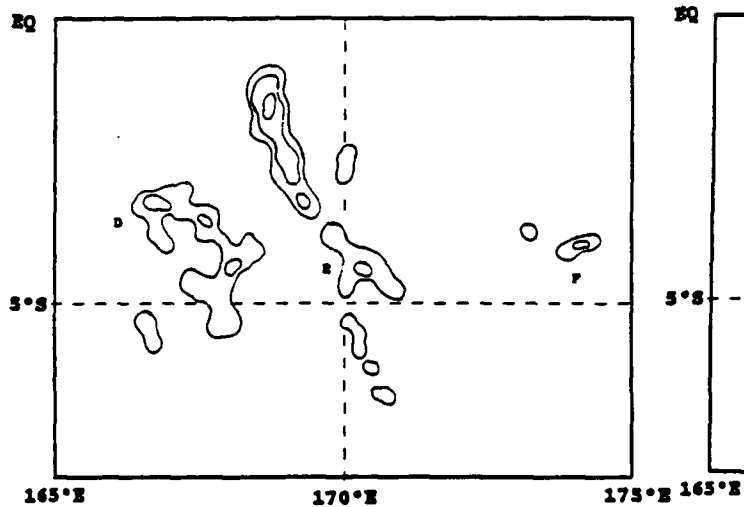
Retrieved values of rainfall RR for this formative-phase cluster are deceptively small, nowhere exceeding 6 mm/hr (Figure 15b). The instantaneous point rainrates in this highly convective cluster were almost certainly far higher than those indicated here, but because of the small horizontal scale of convective precipitation features, these higher non-uniform rainrates tend to be smoothed out in the satellite's field of view. Comparing SSM/I-derived rainrates with IR temperatures from 0630 UTC (Figure 14a), we note that cloud features "A", "B", and "C", each with IR temperatures $< -65^\circ\text{C}$, have no detectible rainfall associated with them. Time difference alone cannot account for this, since the satellite passes were only 15 minutes apart. It seems most likely that "A", "B", and "C" represent anvil clouds spreading out from decayed CBs. The resulting cirrus is very high and cold, but non-precipitating. Elsewhere, cold cloud tops



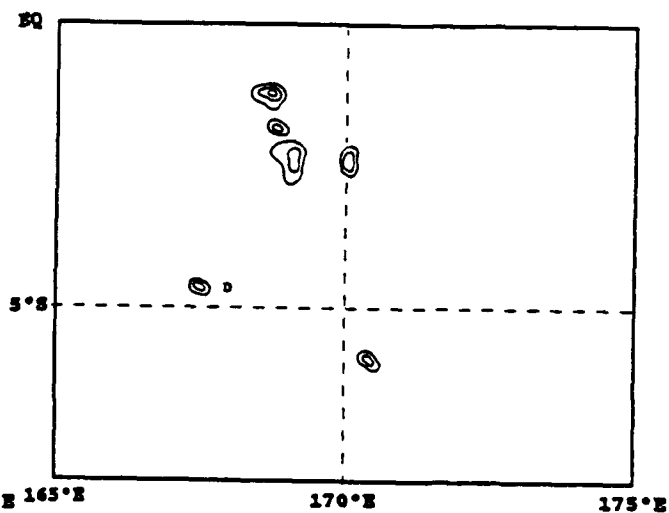
15a.



15b.



15c.



15d.

Figure 15a-d. SSM/I-derived parameters: 13 November 1987 0648 UTC. (a) Integrated water vapor. Units in kg/m^2 . (b) Rainfall. Contours for 0 and 4 mm/hr. (c) Liquid water path. Contours for 500, 1000, 2000 g/m^2 . (d) Ice water path. Contours for 30, 60, 90 g/m^2 .

generally coincide with areas of surface rainfall, as expected in areas of active convection.

Comparison of fields of LWP and IWP indicates the variable microphysical makeup of individual cumulonimbus cells in this formative-phase cluster. LWP maxima "D", "E", and "F" (Figure 15c) have very little corresponding ice content. Conversely, IWP maximum "D" (Figure 15d) is associated with only a modest amount of liquid water.

More precise calibration of relative amounts of liquid water and ice in a TCC is possible in cross sections. Line A in Figure 16 intersects several convective cells. In the resulting cross section along this line (Figure 17), the cell at 167.9°E registers a high ratio of ice to liquid water, while the cell at 170°E , with nearly the same LWP, is almost devoid of large ice particles. It would appear from these results that the two cells were in various stages of growth when SSM/I passed over. Negligible ice content is expected in updrafts of very young cells, prior to glaciation. On the other hand, a balance of ice and liquid water amounts is characteristic of mature CBs, where supercooled water droplets have had time to freeze.

Comparing PCTs derived from high-resolution 85 GHz data to PCTs derived from low-resolution (averaged) 85 GHz data along the same cross section (Figure 18) shows the profound effect of beamfilling. Three abrupt minima in high-resolution PCT, each corresponding to deep ice scattering by glaciated convective cells, are muted at lower resolution--the middle

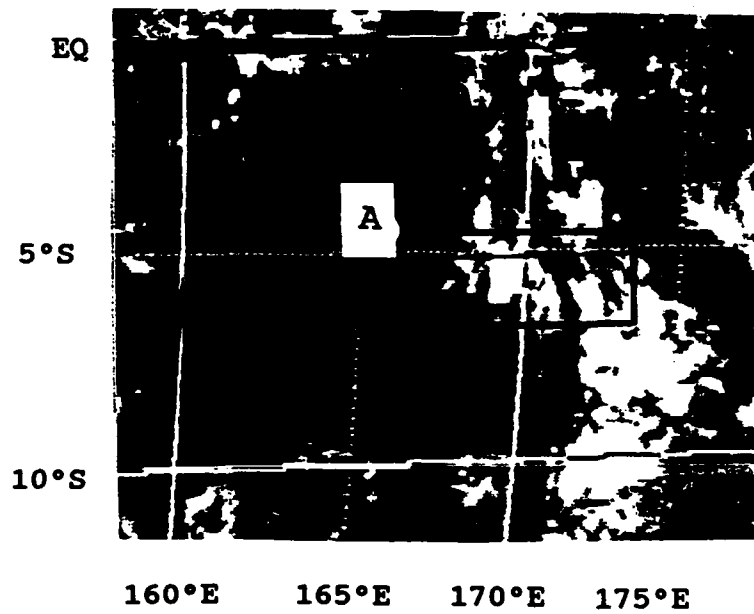


Figure 16. GMS unenhanced IR: 13 November 1987 0330 UTC.

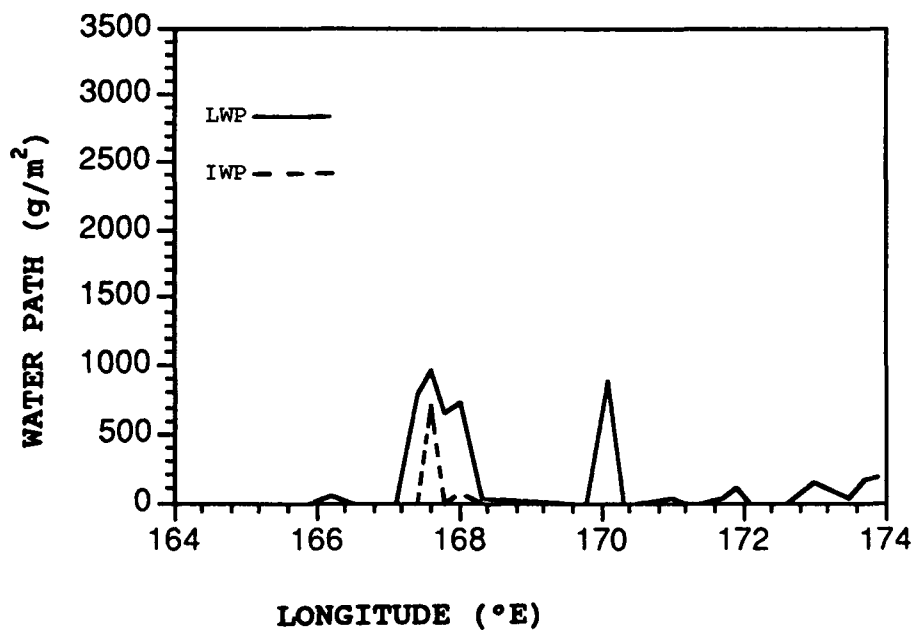


Figure 17. Cross section of LWP and IWP: 13 November 0648 UTC. Along 4.56°S.

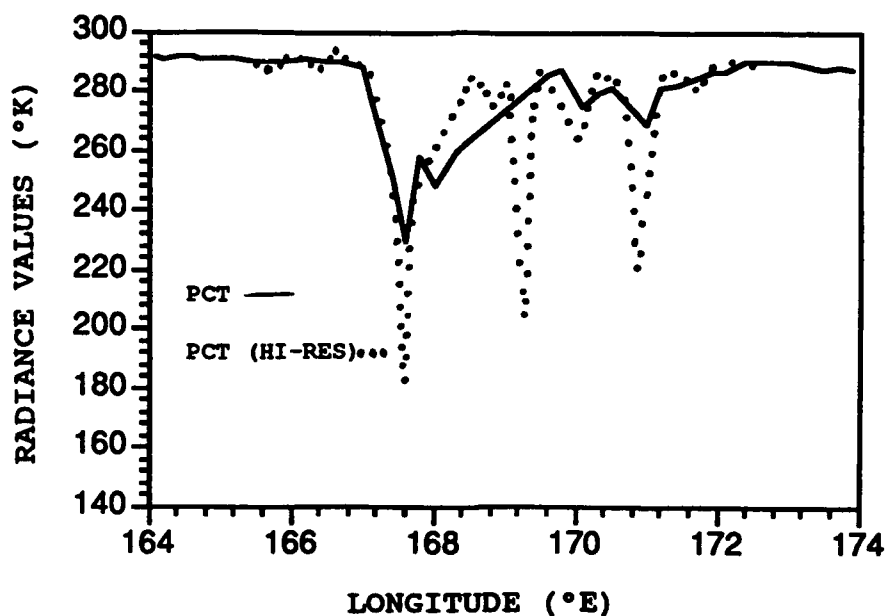


Figure 18. Cross section of PCT: 13 November 1987 0648 UTC. Along 4.56°S.

depression at 169°E is wiped out entirely. Again, horizontal smoothing is characteristic of the response of SSM/I to small-scale convective cells.

Later in its development the cluster developed an extensive cloud shield, appearing as a bright cloud mass in unenhanced GMS imagery (Figure 19). The F-8 pass from 1927 UTC captured this cluster roughly 2 hours past peak maturity. Figure 20a-e depicts SSM/I-derived parameters from that time.

The field of integrated water vapor V derived from the 1927 UTC SSM/I data (Figure 20a) indicates a very moist region surrounding the

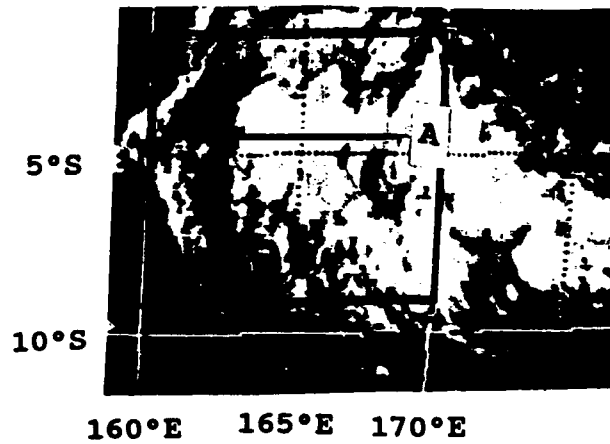


Figure 19. GMS unenhanced IR: 13 November 2130 UTC.

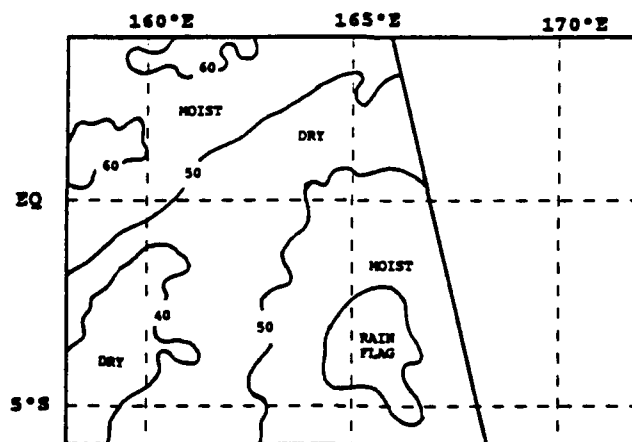
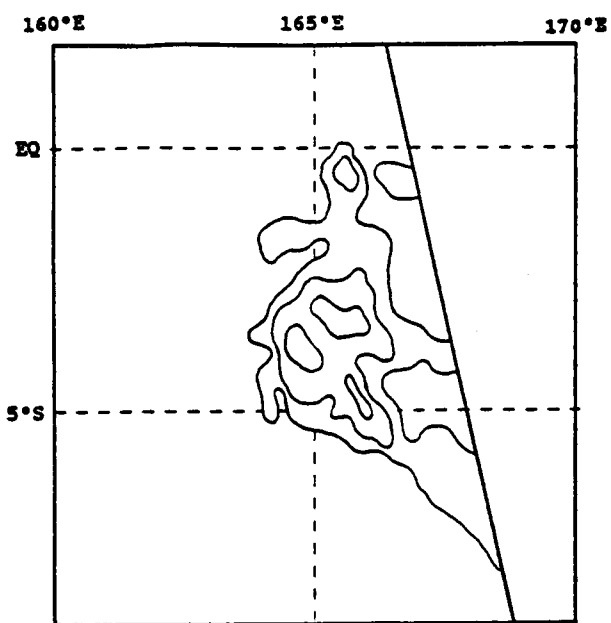
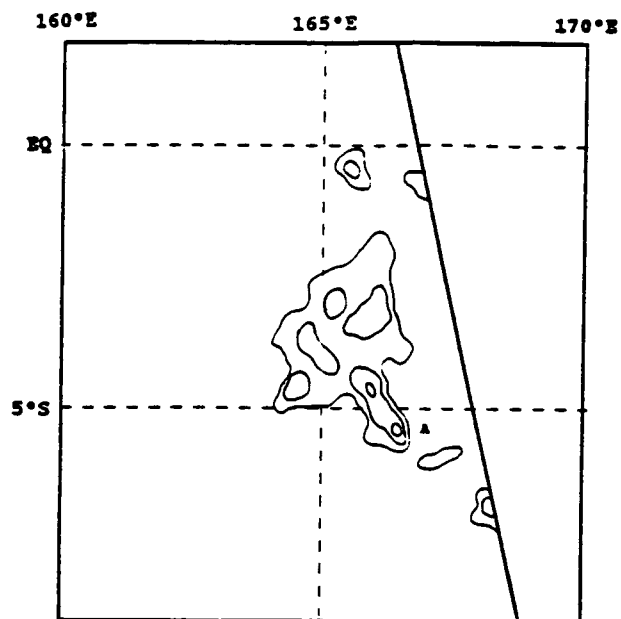


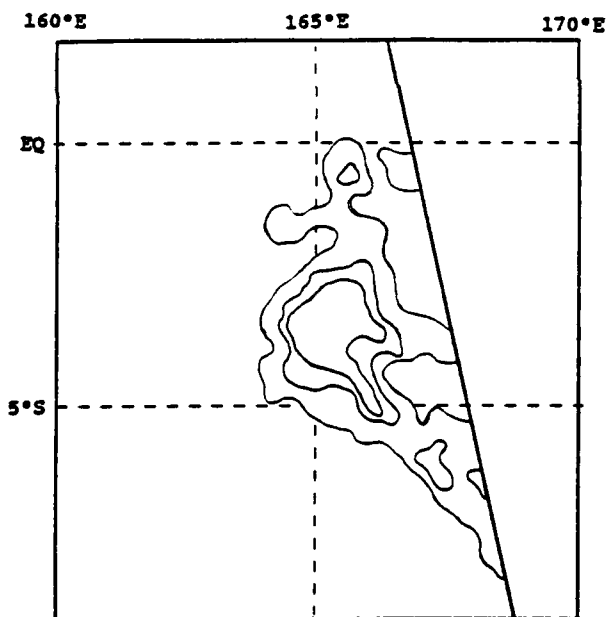
Figure 20a. SSM/I-derived parameters: 13 November 1987 1927 UTC. Integrated water vapor. Units in kg/m^2 . (Cont'd on following page.)



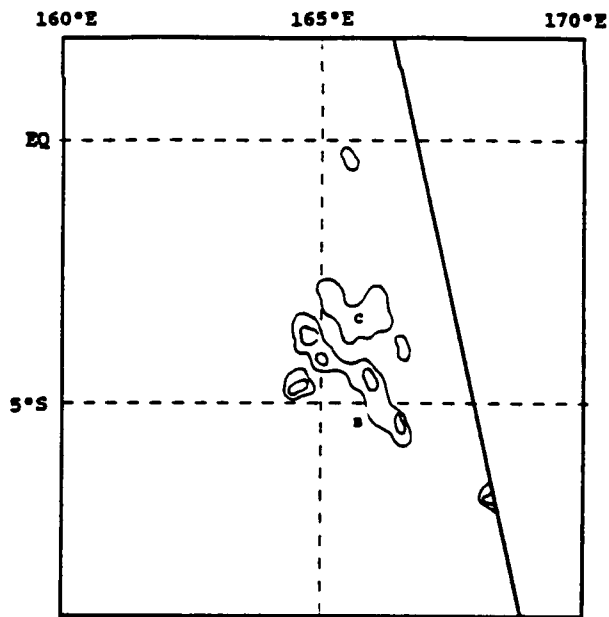
20b.



20c.



20d.



20e.

Figure 20b-e. SSM/I-derived parameters: 13 November 1987 1927 UTC.
(b) Rainfall. Contours for 0, 6, 12 mm/hr. (c) Polarization corrected temperature. Contours for 250°, 230°, 210°K. (d) Liquid water path. Contours for 500, 2000, 4000 g/m². (e) Ice water path. Contours for 60, 120 g/m².

mature TCC (indicated by rain flag). Continuity suggests that the moisture area from 12 hours before (see Figure 15a) had been advected westward as the cluster matured. To the north and west of the moisture maximum at 1927 UTC appears a relatively dry region, possibly caused by compensatory subsidence around a region of mesoscale ascent. The field of V at 14 November 2056 UTC (not shown) still indicates a weak residual moisture axis almost a full day after the storm has decayed. Throughout the pre- and post-storm periods, elevated values of integrated water vapor characterize the environment of the cluster.

Comparison of the SSM/I-derived field of RR (Figure 20b) to the IR temperature field from 1830 UTC (Figure 13d) indicates cold cloud tops ($< -65^{\circ}\text{C}$) coinciding closely with areas of rainfall, allowing for the one-hour time discontinuity. Maximum retrieved rainrates are much higher (up to 16 mm/hr) in the mature than in the formative phase, though this is partially an artifact of less beamfilling in the more horizontally uniform rain field of the mature cluster.

It is of interest to note that minima of PCT (feature "A" in Figure 20c), indicating large ice scattering in deep convection, are not coincident with the coldest IR cloud tops. The coldest cloud tops in the 1830 UTC GMS data (Figure 14d) are to be found to the north, over a stratiform region of only moderate PCT depression. Here again, inferences

of rainrate from IR signatures alone can be deceptive when applied to tropical convection.

A large central region of very high LWP (up to a saturation limit of 4500 g/m^2), apparent in the contour map of Figure 20d, is generally matched by substantial values of IWP (Figure 20e). From the IWP field, the most active convective region of this mature cluster appears located to the south along band "B". To the north, smaller values of IWP correspond to an extensive trailing stratiform region (feature "C") separated by a gap of little or no ice scattering.

Close vertical alignment of liquid water with frozen hydrometeors is apparent in cross section through the cluster (line "A" in Figure 18). Along the cross section (Figure 21), two distinct maxima of IWP (near 164.5E and 165.9E) align with peaks of LWP, though relative amounts vary. A matching cross section pairing high- and low-resolution PCT values for the same region (Figure 22) helps establish the scale of the precipitation features. Where depressions of high-resolution PCT are substantially greater than those of low-resolution PCT, as at 164.5E and 165.9E, the feature is assumed to be small-scale convection. Where PCT depressions are largely unaffected by differences in resolution, as between 164.8E and 165.5E, the feature is assumed to be horizontally uniform and stratiform.

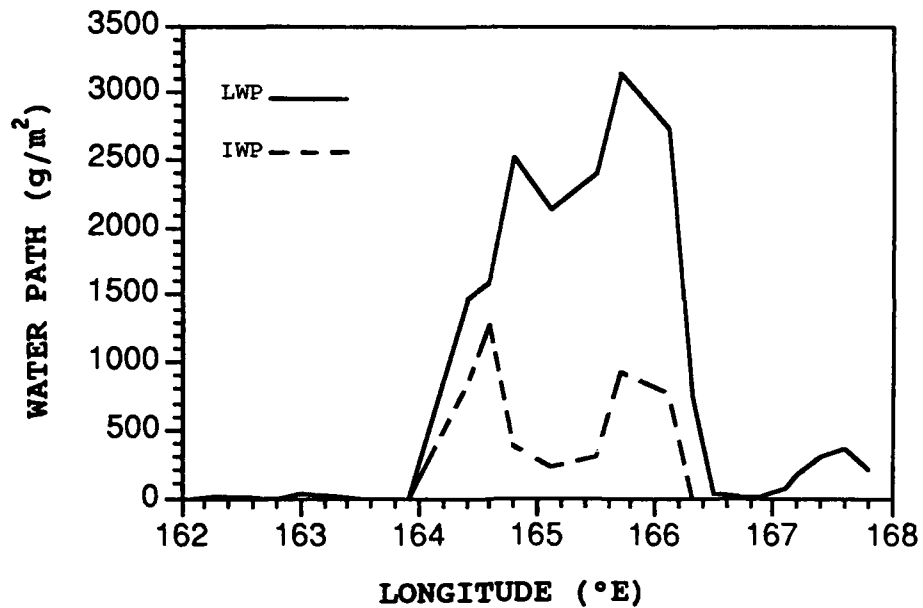


Figure 21. Cross section of LWP and IWP: 13 November 1927 UTC. Along 4.5°S.

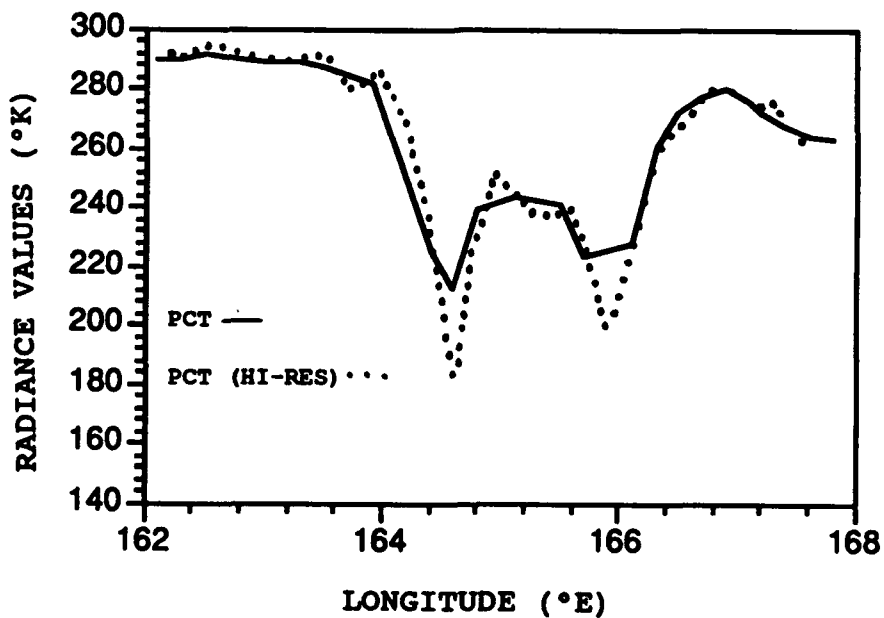


Figure 22. Cross section of PCT: 13 November 1987 1927 UTC. Along 4.5°S.

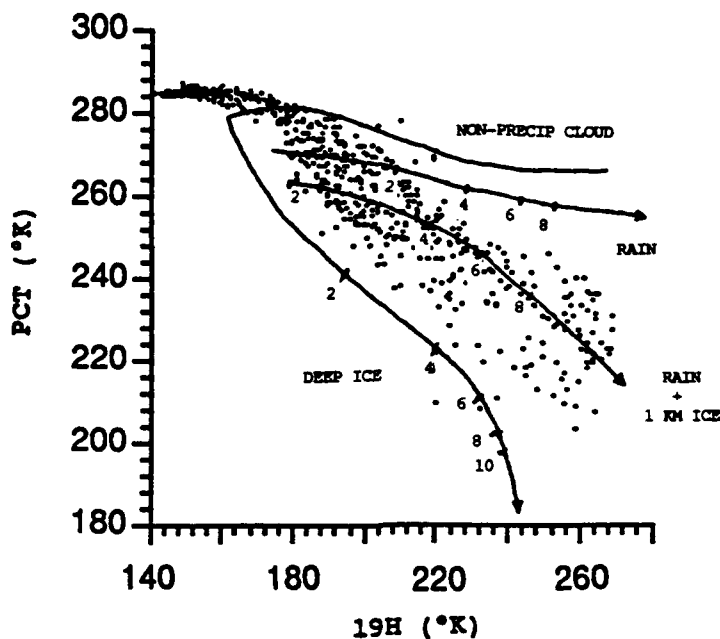


Figure 23. PCT/19H scatter plot: 13 November 1927 UTC. From 6°S to Equator and 162°E to 168°E. Numbers are rainrates in mm/hr.

A scatter plot comparing relative amounts of emission to scattering affords a graphic summary of the predominant microphysical processes in the TCC at its particular growth stage. The plot shown in Figure 23 is comprised of data from the mature cluster at 1927 UTC (outlined by the box in Figure 18). Superimposed on the data are modelled curves taken from Spencer *et al.* (1989). Although these curves are not specifically tuned to the tropics, they do indicate, in a qualitative sense, the effect of an increasingly deep ice layer on microwave radiance values. The upper left-hand portion is the locus of values outside the periphery of the TCC, either

clear sky or thin cloud, where 19H values are at a minimum and PCTs at a maximum. Areas of increasing cloud liquid water and non-ice phase ("warm cloud") precipitation follow curves marked "non-precip cloud" and "rain", respectively. Areas with a precipitating ice layer align with the curves designated "rain + 1 km ice" and "deep ice," depending on the depth of the scattering ice layer and the size of the frozen particles. Each curve is marked with a scale of modelled rainrates (in mm/hr) for the particular microphysical regime. A cursory inspection of the plot indicates most of the "raining" data points in the mature TCC congregate near the "rain + 1 km ice" curve, with a few outliers near or below the "deep ice" curve.

For comparison, a scatter plot was made for the TCC in its formative phase at 0642 UTC (Figure 24). The area of data points is outlined by the box in Figure 16. The distribution of data points in the formative-phase cluster reveals a substantially different microphysical profile: most precipitating pixels appear near or below the "deep ice" curve. From these plots, we conclude most rain falling from the TCC in its formative, purely convective phase was produced in a deep layer of large ice (graupel) particles, with relatively little liquid water emission. As the storm matured, evolving into a mixture of convective and stratiform cloud, rain was produced from a composite of ice and liquid layers.

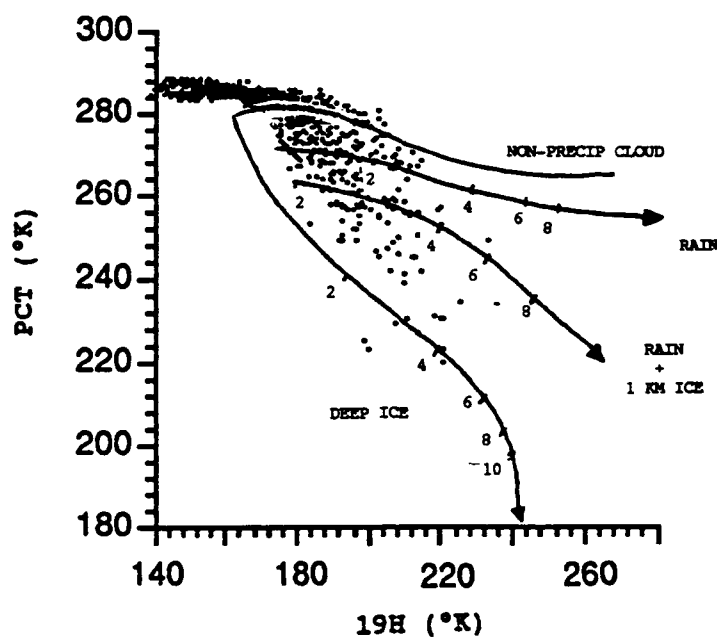


Figure 24. PCT/19H scatter plot: 13 November 0648 UTC. From 7°S to Equator and 165°E to 173°E. Numbers are rainrates in mm/hr.

5.2 TCC of 16 November 1987--Intensifying Phase

On 16 November 1987, a large tropical cloud cluster developed in the western Pacific, between 165°E and 171°E and 3°N and 9°N, as identified by the bright cirrus cloud shield in GMS unenhanced IR imagery (see Figure 25). It grew rapidly from an initial cluster of cumulonimbus cells, and by 1200 UTC had acquired an extensive cold cloud shield. From 1830 to 2130 UTC the $< -65^{\circ}\text{C}$ cloud shield changed very little in areal extent (see Figure 26a-b for contours of IR temperatures), although the 1830 UTC analysis depicts a tighter centroid of very cold ($< -85^{\circ}\text{C}$) cloud tops. Interpolating

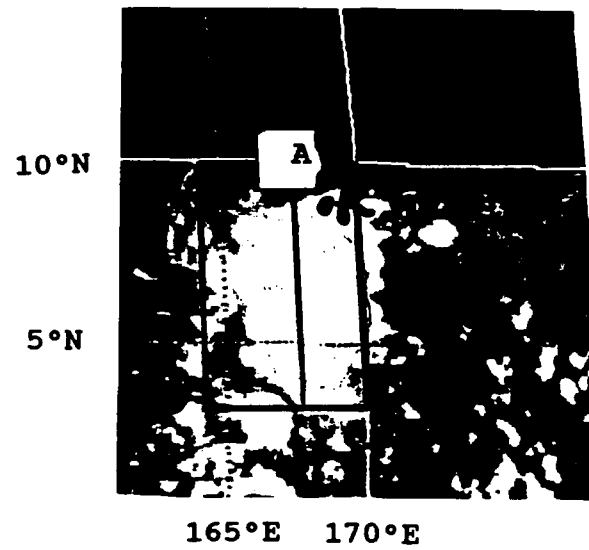


Figure 25. GMS unenhanced IR: 16 November 1987 2130 UTC.

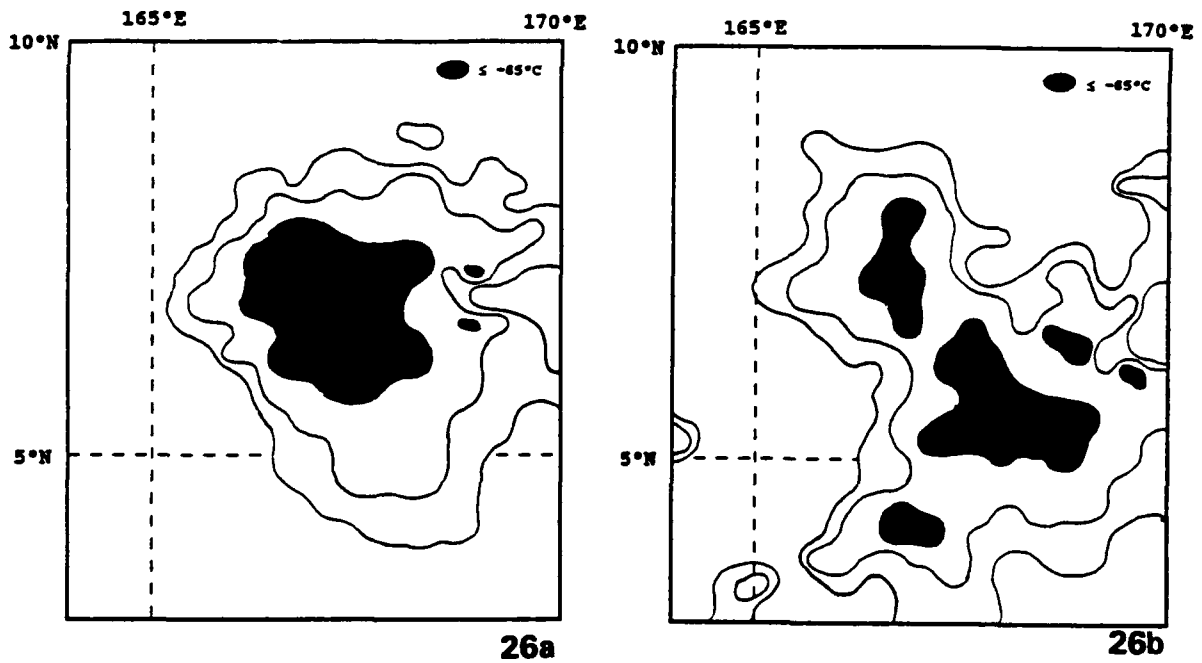


Figure 26a-b. GMS IR temperatures: 16 November 1987. Contours for -65°C , -75°C , -85°C . (a) 1830 UTC (b) 2130 UTC.

between the two times, it was estimated the cluster reached peak maturity at 2000 UTC.

ECMWF 850mb wind vectors (not shown) depict synoptic scale convergence between 165°E and 167°E during the pre-storm phase. At 200mb, anticyclonic flow is indicated over the region of the maturing TCC. The combination of low-level convergence and upper level anticyclonic flow enhanced vertical motions on the synoptic scale, making this a favored region for convective development.

SSM/I-derived fields of columnar water vapor V from 14 November 1914 UTC, 15 November 1902 UTC, and 16 November 1850 UTC (not shown) indicate a very moist environment prevailing up to 48 hours before TCC development. Values of V within each SSM/I data swath are uniformly in excess of 55 kg/m².

SSM/I's 1850 UTC pass time on 16 November occurred roughly one hour before estimated peak maturity of the TCC, thus capturing a cluster in the intensifying phase. Fields of SSM/I-derived RR, PCT, LWP, and IWP are analyzed in Figure 27a-d. Because of the small time difference, it is instructive to compare closely the field of SSM/I-derived rainfall from 1850 UTC (Figure 27a) to the nearly-coincident field of IR cloud-top temperatures from 1830 UTC (Figure 26b). As is apparent from the analyses, retrieved surface rainfall correlates well with the -65°C contour of IR cloud-top temperatures. Regions of heavier rain, up to 15 mm/hr, are generally

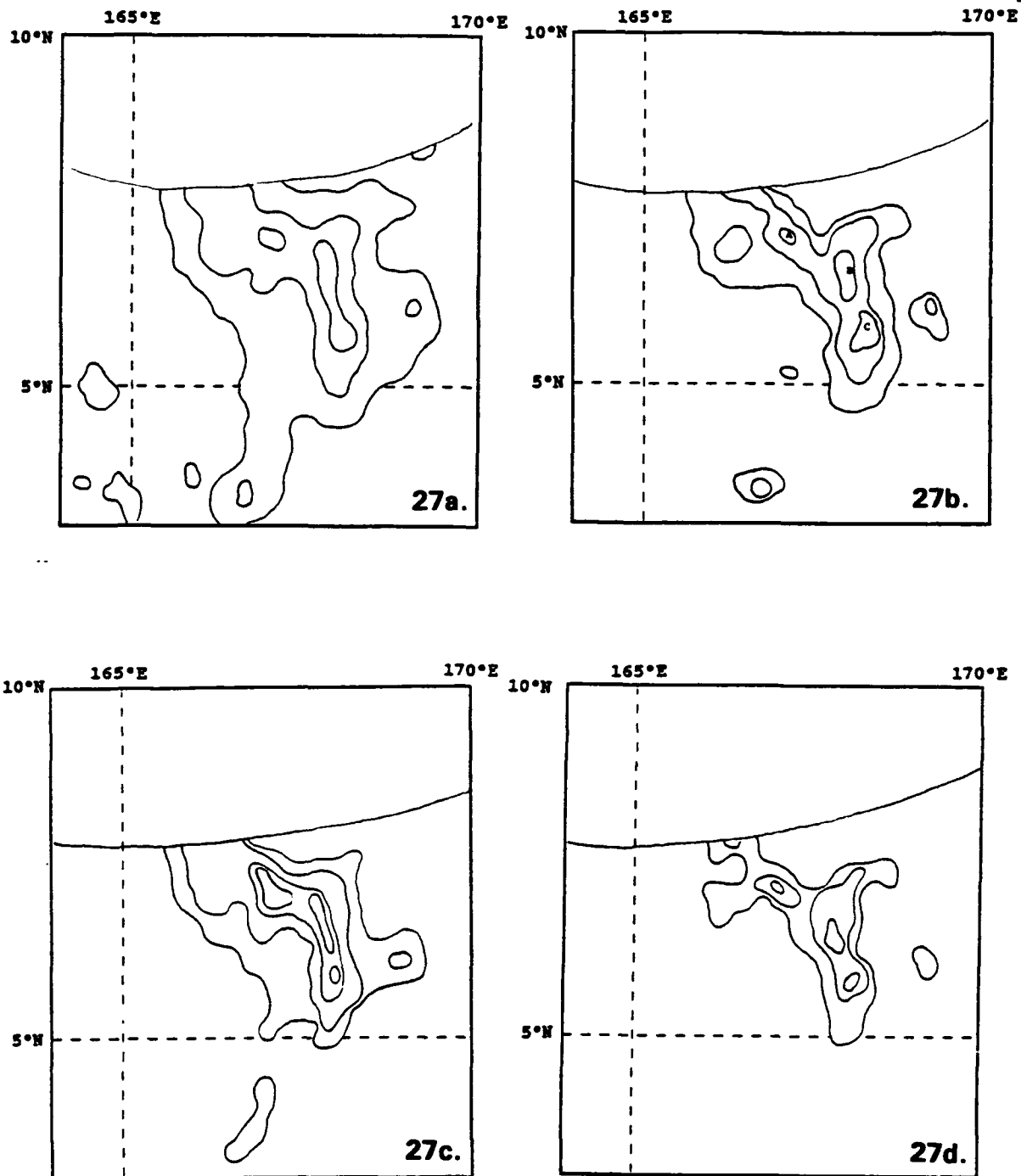


Figure 27a-d. SSM/I-derived parameters: 16 November 1987 1850 UTC. (a) Rainfall. Contours for 0, 6, 12 mm/hr. (b) Polarization corrected temperature. Contours for 250°, 230°, 210°K. (c) Liquid water path. Contours for 1000, 2000, 3000, 4000 g/m². (d) Ice water path. Contours for 50, 100, 150 g/m².

co-located with the coldest ($< -85^{\circ}\text{C}$) IR temperatures, although very cold tops are found in regions of light precipitation as well.

The field of PCT (Figure 27b) indicates three minima, marked "A", "B", "C", where ice scattering is especially pronounced. These deep depressions, all below 200°K , correspond to strong convective cells, which are to be expected in a still-growing TCC. More extensive regions of moderate PCT depressions, corresponding to lighter stratiform precipitation, are located to the south and to the west of central convection. A band of maximum LWP values also appears through the center of the cluster (Figure 27c), and is generally coincident with areas of maximum IWP (Figure 27d).

A cross section analysis reveals the close correlation of liquid water emission with ice scattering through the center of the cluster (Figure 28). Along the same cross section, the profound depression of high-resolution PCT values at 6.5°N is almost entirely smoothed out in the lower resolution data (Figure 29). This discrepancy is characteristic of an intense, narrow convective line. To the south, between 5°N and 6°N moderate PCT depressions are indicative of stratiform precipitation.

The overall microphysical profile of this intensifying-phase TCC is graphically presented in a PCT versus 19H scatter plot (Figure 30), from the area outlined by the box in Figure 25. It will be noted that most raining pixels lie midway between those of the 13 November cluster in its formative

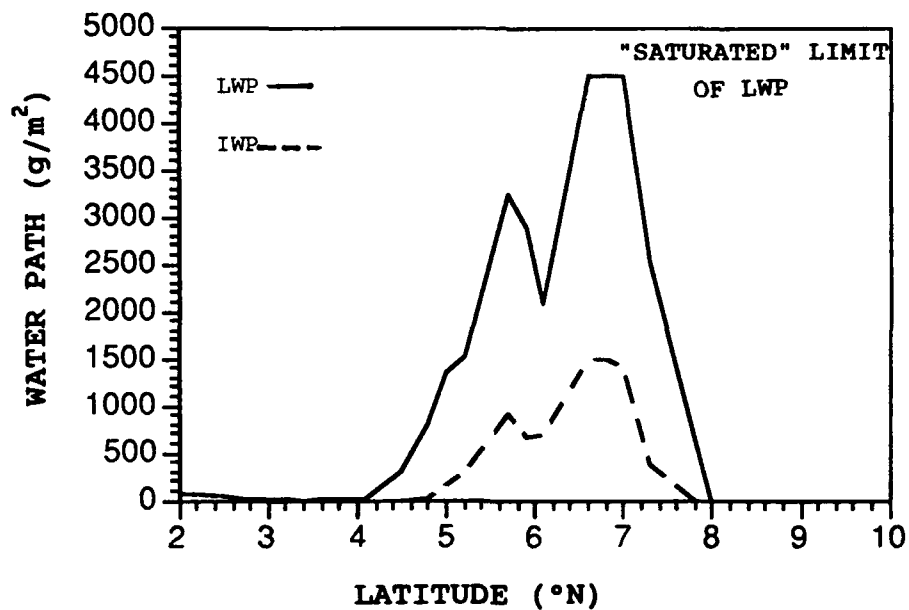


Figure 28. Cross section of LWP and IWP: 16 November 1987 1850 UTC. Along 167.8°E.

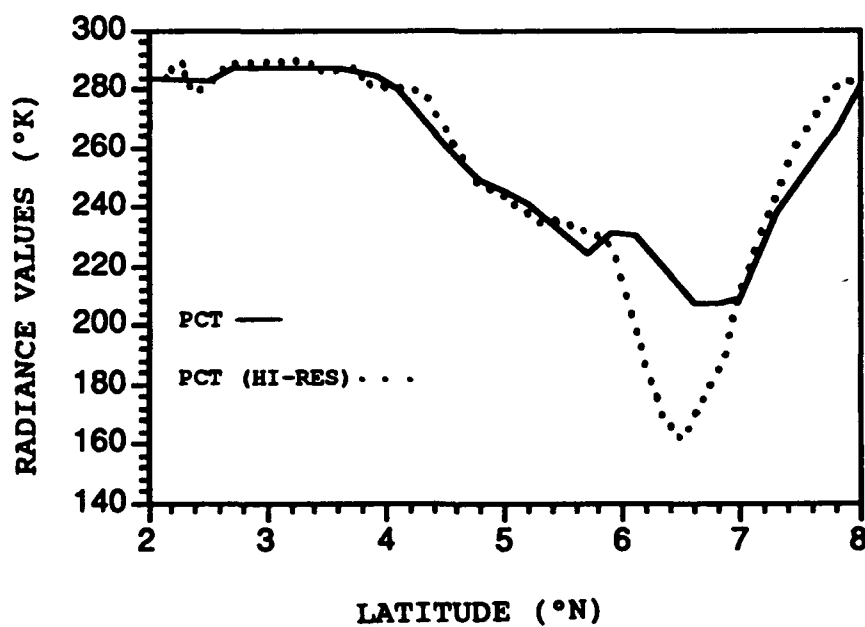


Figure 29. Cross section of PCT: 16 November 1987 1850 UTC. Along 167.8°E.

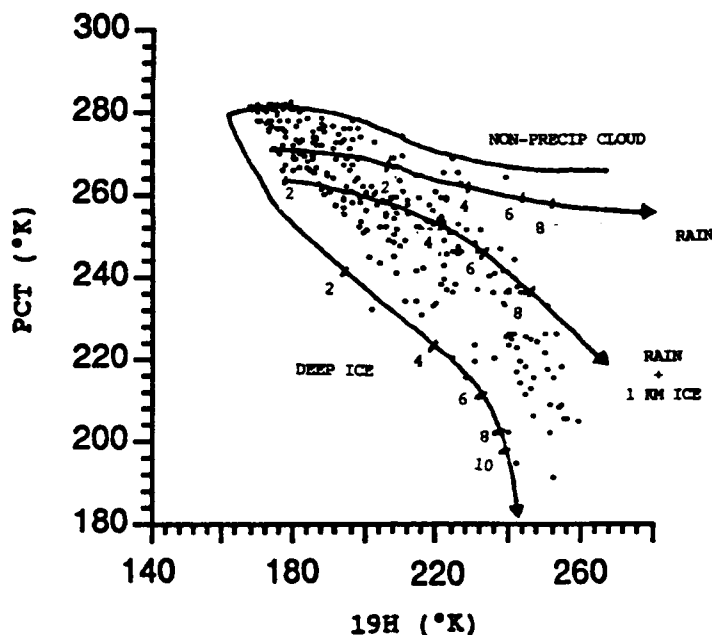


Figure 30. PCT/19H scatter plot: 16 November 1987 1850 UTC. From 4°N to 8°N and 165°E to 169°E. Numbers are rainrates in mm/hr.

phase (Figure 24) and mature phase (Figure 23)--that is, between the curves marked "deep ice" and "rain + 1 km ice".

5.3 TCC of 21 November 1987--Dissipating Phase

On 21 November 1987 an area of enhanced convection appeared along a feeder band of Typhoon Nina. As Nina pulled off to the west, this convective area evolved independently and developed a mesoscale cirrus canopy, appearing as a very bright cloud mass on unenhanced GMS imagery

(Figure 31). From the areal extent of the -65°C cloud shield it was estimated the TCC reached peak maturity around 1530 UTC. Between 1830 UTC and 2130 UTC, the mesoscale cloud shield warmed considerably as the cluster decayed (compare IR analyses in Figures 32a-b). By 0030 UTC the cloud shield disappeared altogether.

Synoptic conditions in the wake of Typhoon Nina appear to have favored convective development, with anticyclonic circulation aloft, and weakly convergent flow at low levels in the genesis region of the TCC. In addition, fields of integrated water vapor V from 19 November 1955 UTC,

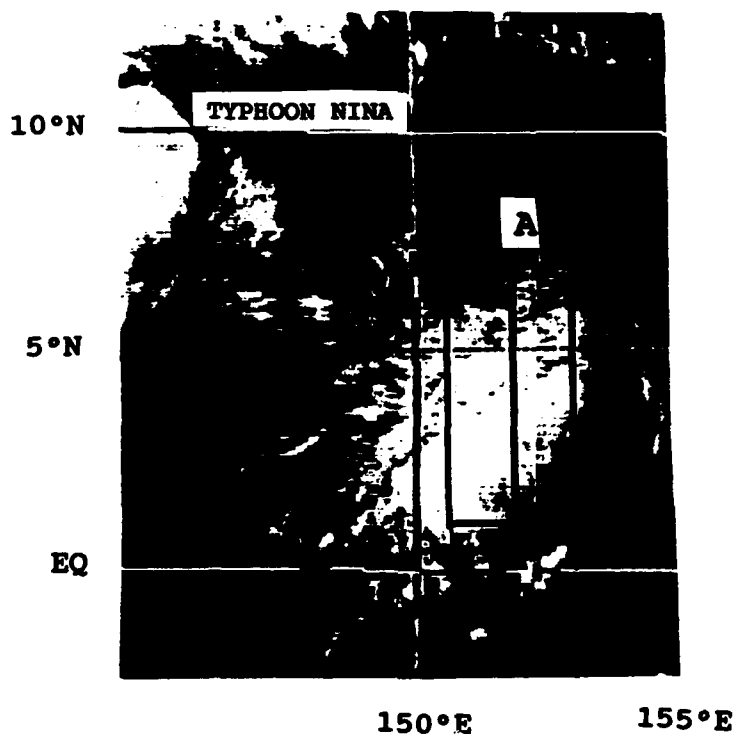


Figure 31. GMS unenhanced IR: 21 November 1987 2130 UTC.

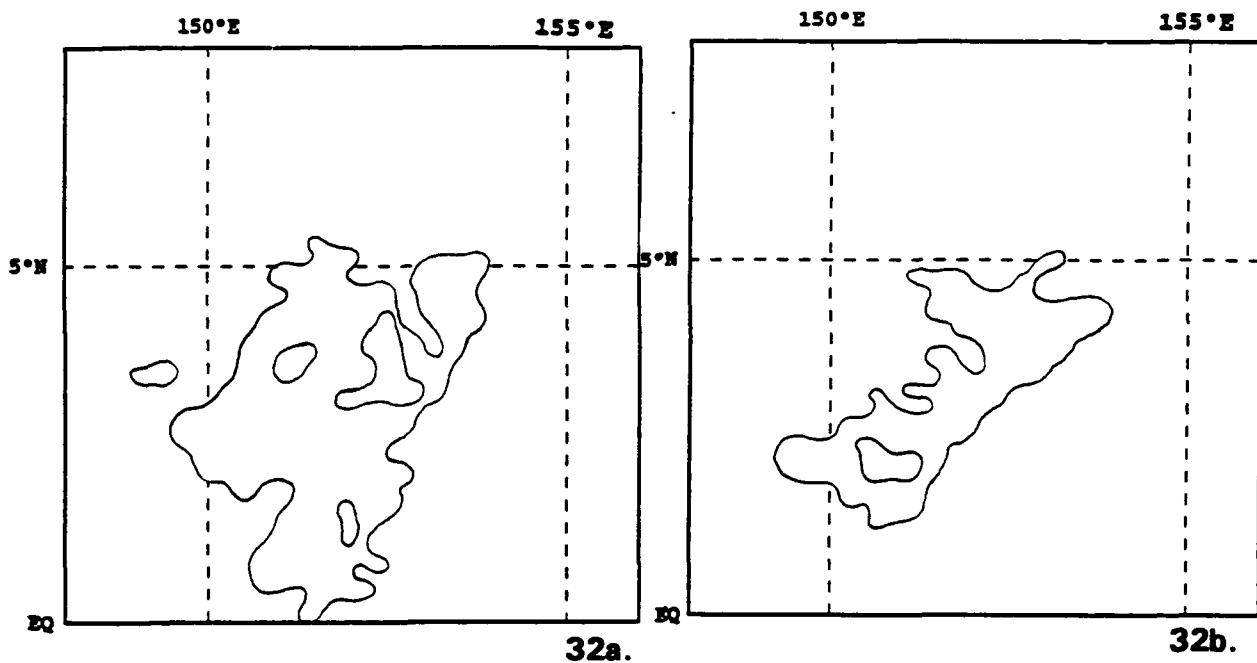
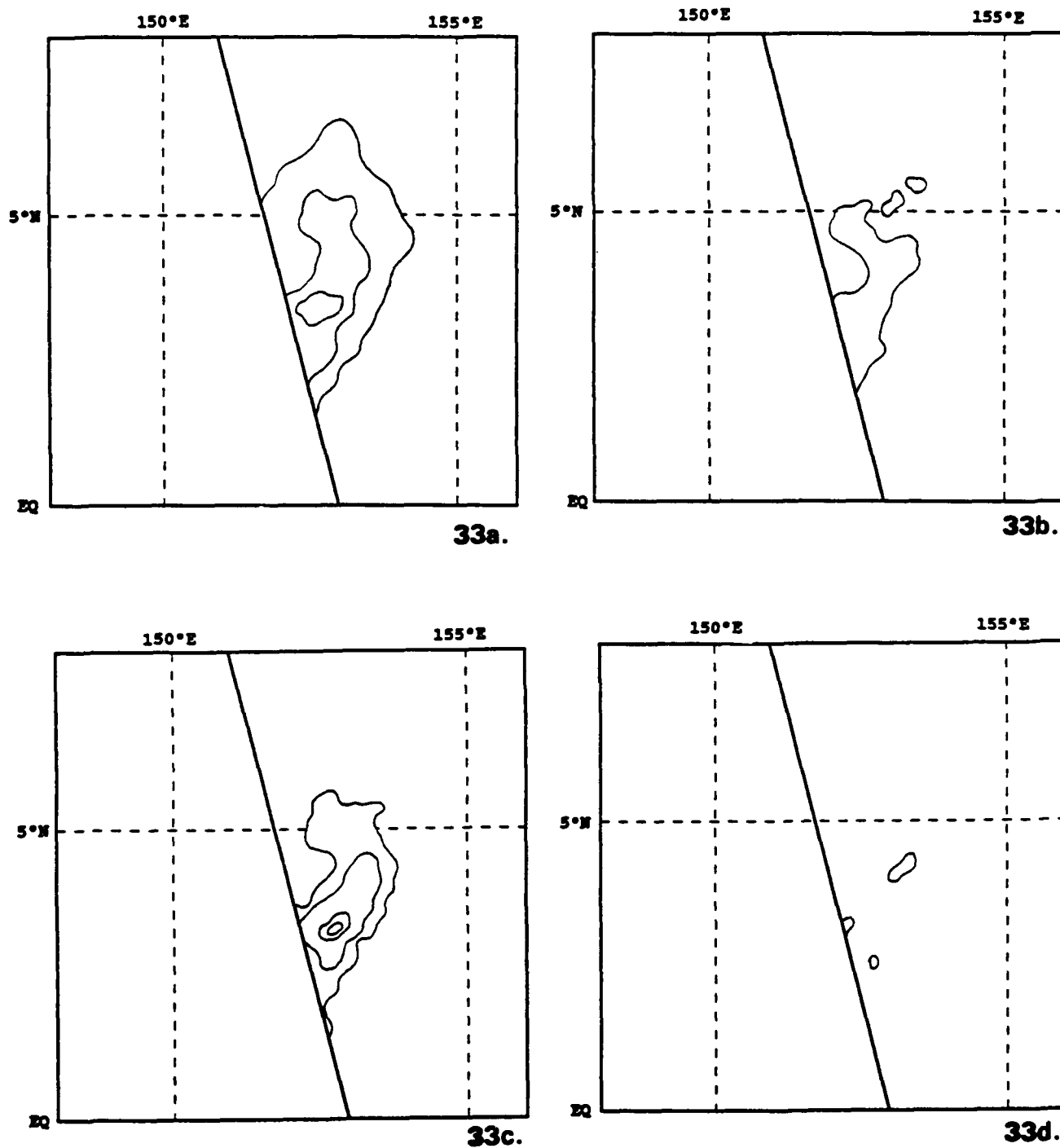


Figure 32a-b. GMS IR temperatures: 21 November 1987. Contours for -65°C, -75°C. (a) 1830 UTC (b) 2130 UTC.

20 November 1942 UTC, and 21 November 1930 UTC indicate an unusually moist environment, with values of V greater than 55 kg/m^2 throughout the entire region. Because these fields are uniformly moist, with negligible moisture gradients, they are not shown.

An SSM/I pass time of 1930 UTC on 21 November recorded the TCC roughly 4 hours past peak maturity. At this time, the cluster still displayed an extensive, though rapidly-shrinking cold cloud shield. Fields of SSM/I-derived RR, PCT, LWP, and IWP (Figure 33a-d) provide a telling



contrast to the IR cloud signature. Rainfall amounts in the dissipating cluster are uniformly light (nowhere exceeding 9 mm/hr) but very extensive, even with the SSM/I data swath missing a substantial part of the cluster. An area of light rain to the north of 5N coincides with cloud-top temperatures warmer than -65°C . Gradients of PCT (Figure 33b) are slight. Widespread modest depressions of PCT, nowhere less than 245°K , is the characteristic scattering signature of stratiform precipitation where the ice layers consist of smaller, primarily soft ice particles. Curiously, values of LWP are still considerable, with a local maximum of $> 4000 \text{ g/m}^2$ (Figure 33c). Values of IWP, however, are negligible, nowhere exceeding 60 g/m^2 (Figure 33d).

A cross section through the center of the cluster along line "A" in Figure 31 depicts negligible IWP coupled with large values of LWP (Figure 34). The stratiform character of the cluster in this stage of development is evident from a cross section through the same area, comparing low- and high-resolution values of PCT (Figure 35). In a horizontally uniform rain field differences of resolution have little effect on the amount of ice scattering detected, as here, where PCTs remain between 240°K and 250°K regardless of the resolution of the data.

The relative preponderance of liquid water over large frozen particles in the entire TCC is presented graphically in a scatter plot of PCT versus 19H values (Figure 36) comprising the region outlined by the box in

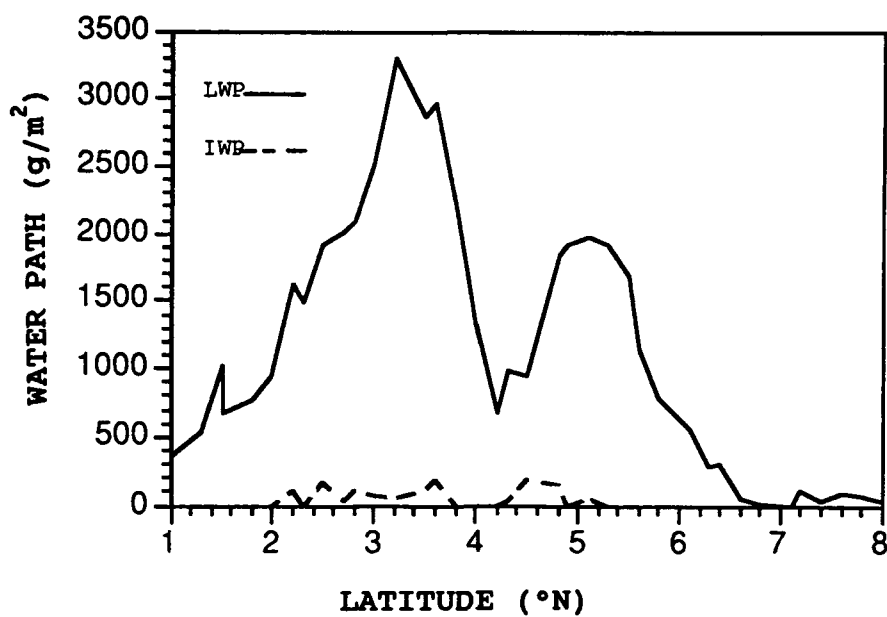


Figure 34. Cross section of LWP and IWP: 21 November 1987 1930 UTC. Along 152.6°E .

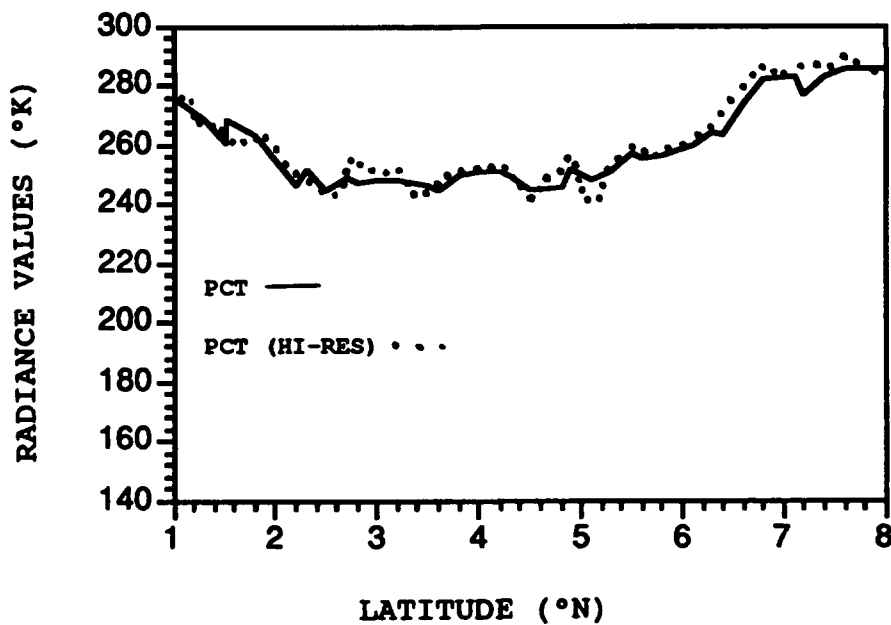


Figure 35. Cross section of PCT: 21 November 1930 UTC. Along 152.6°E .

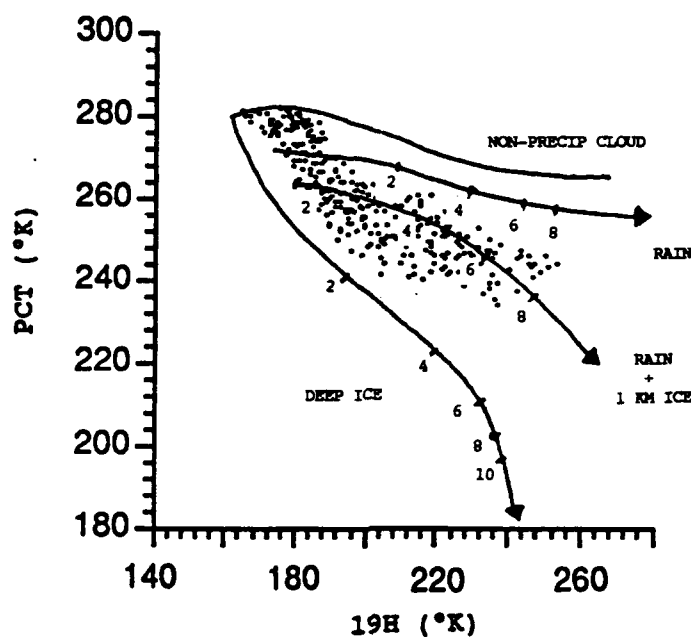


Figure 36. PCT/19H scatter plot: 21 November 1930 UTC. From 1°N to 7°N and 151°E to 154°E. Numbers are rainrates in mm/hr.

Figure 31. Compared to similar scatter plots made from TCCs in earlier stages of development (see Figures 23, 24, 30), the raining data points in this dissipating cluster congregate near and above the "rain + 1 km ice" curve, some even approaching the (warm) rain curve. Overall, the series of scatter plots indicates that the relative amount of liquid water versus large frozen hydrometeors changes considerably in the course of TCC development from a predominantly convective to a predominantly stratiform phase.

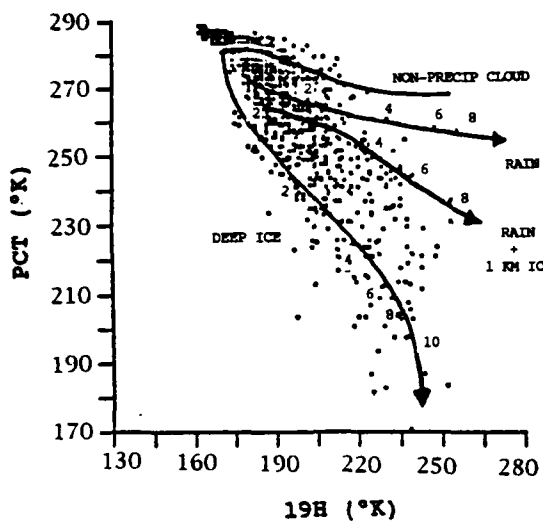
CHAPTER 6

DISCUSSION

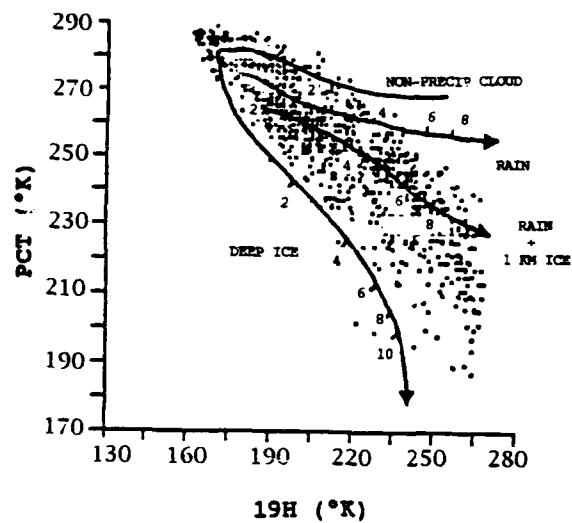
In the preceding case studies of evolving TCCs we note a decided change of a cluster's overall microphysical profile through the course of development. This change may be briefly summarized as follows:

1. **Formative stage:** rain mainly produced by isolated CBs consisting of deep ice layers of large graupel, but comparatively little liquid water.
2. **Mature stage:** convective CBs and stratiform cloud co-exist, rain area is extensive, with ice layers deeper in CBs than in stratiform rain area, and large values of liquid water.
3. **Dissipating stage:** as CBs disappear, remaining stratiform clouds continue to rain lightly. The deep ice layer within the stratiform cloud shield consists of smaller particles, resulting in less pronounced microwave scattering than in the formative and mature stages.

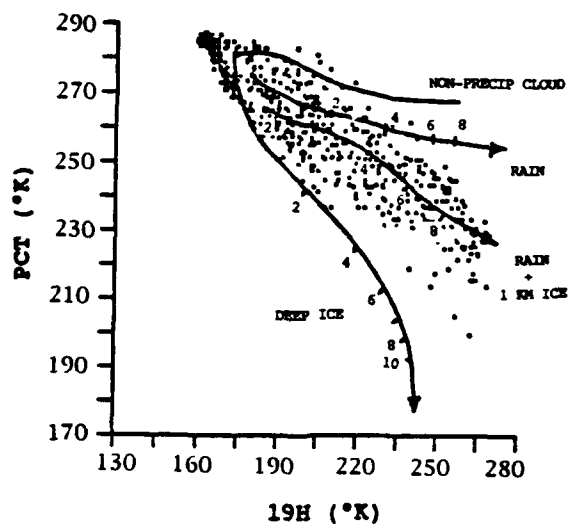
These conclusions from individual cases are borne out in composite scatter plots of PCT versus 19H in Figure 37a-c. Each of these plots represents a composite of 5 TCCs in a particular stage of development: formative (from generation of mesoscale cloud shield to 2 hours before peak), mature (within 2 hours of peak), and dissipating (from 2 hours after



37a.



37b.



37c.

Figure 37a-c. Composite PCT/19H scatter plots. Numbers are rainrates in mm/hr. (a) Formative TCCs. (b) Mature TCCs. (c) Dissipating TCCs.

peak until decay of cloud shield). As in individual cases, we note that the raining data points drift from below the "deep ice" curve to near and above the "rain + 1 km ice" curve as clusters evolve.

The results shown in both case studies and composite plots are consistent with findings of Houze and Churchill (1984) that stratiform regions of TCCs contain much lower concentrations of ice than do convective cells. In the plot of dissipating, predominantly stratiform TCCs, less ice scattering is observed than in the plot of growing convective clusters.

On the other hand, it is notable that dissipating TCCs display such large values of liquid water emission coupled with negligible ice scattering. In Houze's model of the TCC life cycle (1982) clusters decay from the surface up, at the end consisting of nothing but a weakly precipitating ice layer well above the freezing level (see Figure 38c). The results from this study suggest that the stratiform cloud deck of a dissipating system contains ice particles of comparatively small radius. While these frozen hydrometeors are still precipitating, as evidenced by the large values of liquid water path from below the freezing level, the relatively modest ice scattering is evidence of smaller-sized particles, and generally lower ice mixing ratio as compared to the convective phase.

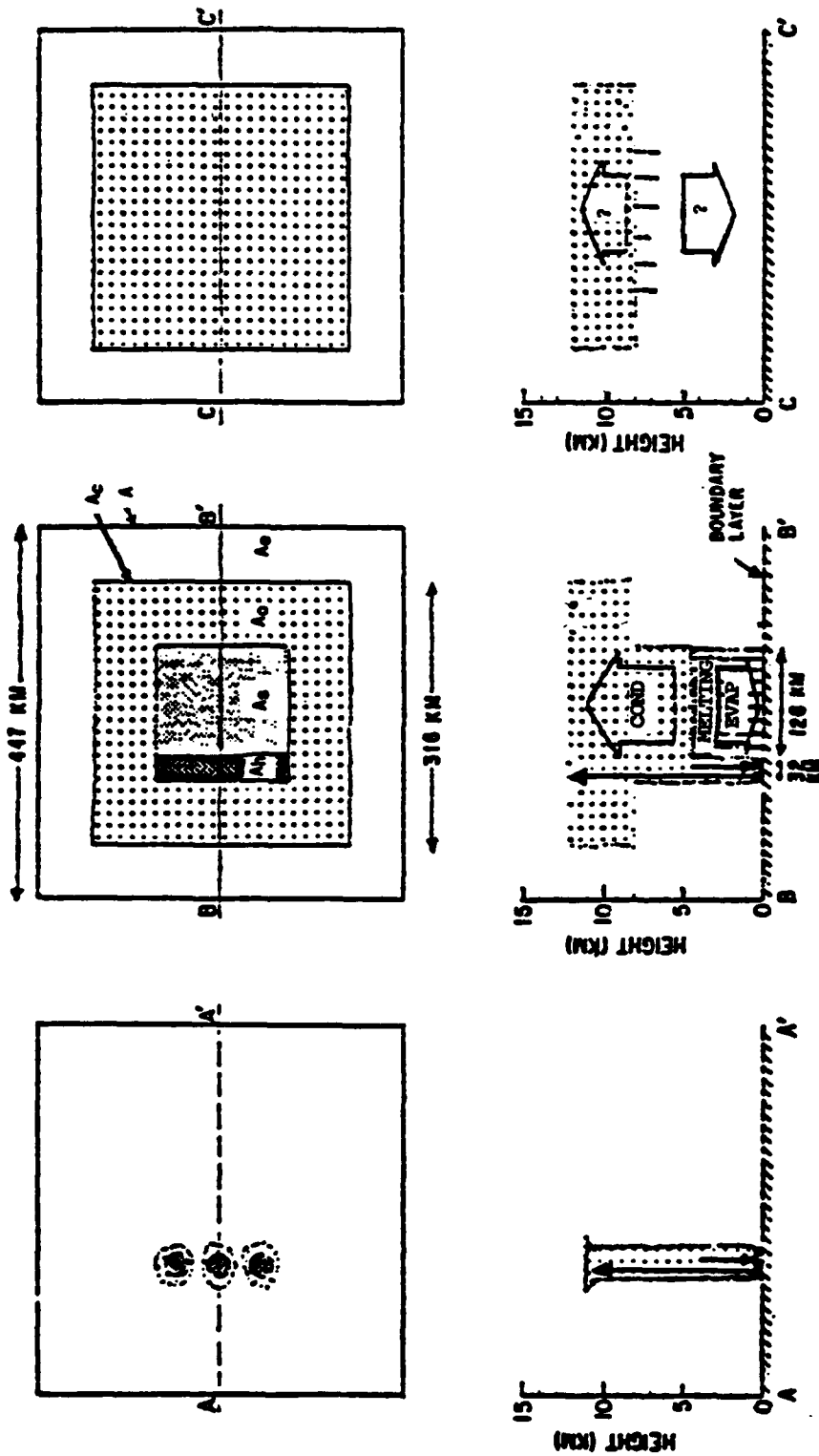


Figure 38a-c. Schematic of a tropical cloud cluster in three successive stages of development. (a) Formative stage consisting of convective cells. (b) Mature stage. Cloud shield covers area A_0 , convective cells are located in area A_h , stratiform precipitation falling from mid-level cloud base within area A_0 and A_h is covered by upper-level cloud overhang. (c) Dissipating stage in which convective cells have disappeared and weak stratiform precipitation is not reaching ground. Upper panels of (a) - (c) are plan views. Lower panels are vertical cross sections. Source: Houze (1982).

It is noteworthy that the largest amount of ice scattering in tropical maritime convection is found to be substantially less than that reported for midlatitude thunderstorms. In none of the cases examined did depressions of 37H brightness temperature approach the value of 163°K reported by Spencer *et al.* (1983) for a thunderstorm in the Great Plains, even though vertical development of tropical systems is very deep, as indicated by extremely cold IR cloud top temperatures. Less ice scattering is consistent with findings of LeMone and Zipser (1980) that updraft speeds in tropical convection are much lower than in continental thunderstorms of the midlatitudes. Lower updraft speeds would tend to support smaller particles of hail and graupel, resulting in smaller scattering depressions.

CHAPTER 7

CONCLUSION AND RECOMMENDATIONS FOR FURTHER STUDY

From the analysis of 15 western Pacific tropical cloud clusters using SSM/I data, the following conclusions may be tentatively advanced:

- areas of precipitation in TCCs conform reasonably well to the -65°C IR contour. However, the coldest cloud tops do not necessarily coincide with regions of heaviest rain.
- TCCs evolve through an initial, predominantly convective phase to a late, predominantly stratiform phase. In mature clusters, still-active convective cells, either linearly or randomly distributed, were found imbedded in stratiform precipitating clouds of large horizontal extent.
- the pre-storm environment of tropical cloud clusters is typified by local maxima of integrated water vapor. Elevated moisture content most likely signals gentle synoptic-scale ascent, although moistening by previous convection may also play a part.
- the microwave signature of a TCC changes over the course of its life cycle, from a balance of liquid water emission and ice scattering in the intensifying and mature phases, to a predominance of liquid water emission over ice scattering in the dissipating phase.

Certainly, a larger number of varied cases would permit a more confident assertion of these conclusions. Still, even with this limited data base it is evident that SSM/I data provides insights into storm structure not available through traditional satellite imagery. It would be most instructive in the future to compare microwave signatures of tropical convection in the western Pacific against the radar, rawinsonde, and aircraft measurements being gathered during the TOGA COARE field experiment. Once available, these data will provide a unique opportunity to calibrate the microwave signatures of tropical cloud clusters, and allow a more rigorous validation of some of the conclusions drawn here.